



CHALMERS
UNIVERSITY OF TECHNOLOGY

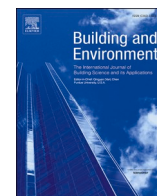
Moisture absorption of an aerogel-based coating system under different wetting scenarios

Downloaded from: <https://research.chalmers.se>, 2024-03-20 09:59 UTC

Citation for the original published paper (version of record):

Karim, A., Sasic Kalagasidis, A., Johansson, P. (2023). Moisture absorption of an aerogel-based coating system under different wetting scenarios. *Building and Environment*, 245.
<http://dx.doi.org/10.1016/j.buildenv.2023.110905>

N.B. When citing this work, cite the original published paper.



Moisture absorption of an aerogel-based coating system under different wetting scenarios

Ali Naman Karim^{*}, Angela Sasic Kalagasidis, Pär Johansson

Department of Architecture and Civil Engineering, Division of Building Technology, Chalmers University of Technology, SE-41296, Gothenburg, Sweden

ARTICLE INFO

Keywords:

Aerogel
Coating mortar
Wetting
Runoff
Capillary suction
Drying

ABSTRACT

Aerogel-based coating mortars (ACM-systems) provide energy-efficient retrofitting solutions for masonry buildings, with thermal conductivities (30–50 mW/(m·K)) comparable to traditional insulation materials. However, limited knowledge on their moisture absorption under rainwater wetting hinders the moisture-safe design of building envelopes incorporating these mortars. Thus, this study investigated the moisture absorption of an ACM-system under three laboratory-created wetting scenarios. A small-scale setup was developed to simulate runoff wetting based on typical wind-driven rain intensities in Sweden, enabling continuous monitoring of moisture conditions during wetting and drying. Two complementary capillary suction experiments under zero (free suction) and elevated hydrostatic pressure explored additional wetting scenarios. The impact of water-repellent paint and surface cracks was also assessed, as previous testing focused on undamaged ACM-systems. Among the three wetting scenarios, runoff wetting resulted in the lowest moisture absorption by the undamaged ACM-system. Water-repellent paint ($s_d = 0.01$ m) reduced moisture uptake by up to 15% during runoff and 50% during free capillary suction for the same system. Horizontal or vertical surface cracks of 1 ± 0.5 mm width increased water absorption by 3–5 times during prolonged runoff wetting, comparable to suction at elevated hydrostatic pressure. Furthermore, a trial was done to verify a simplified numerical moisture transport model using the runoff experiment. The results highlighted the necessity for future model refinement and advanced moisture transport modeling in the ACM-system. The developed small-scale setup facilitated easy use and real-time monitoring of moisture conditions during wetting and drying. Future development should include wind-driven rain simulation alongside the existing runoff wetting scenario.

1. Introduction

Protection against water leakage from precipitation is a fundamental performance criterion for building envelopes [1–6]. Failure to maintain the integrity in this regard leads to significant financial consequences annually. To control rainwater intrusion, strategies like water repellent surface treatments, ventilated layers behind façades, and leveraging the moisture buffering capacity of building materials are commonly employed [2,7]. However, numerous factors influence the envelope's performance in practice. Recent and widespread serial failures, like the introduction of external thermal insulation composite system (ETICS) on wooden constructions in Sweden, highlight the complexities of introducing tested materials and solutions to new markets [8,9]. In this case, the external coating mortar system failed to prevent water leakage, causing damage to the wooden structure within the building envelope. Similar serial failures, including structural deterioration and

compromised integrity against rainwater leakage have occurred in buildings in Canada [10] and New Zealand [11], resulting in significant water intrusion, mold growth, rot, and interior damage. These failures incurred substantial repair costs and negatively impacted on the construction industry's reputation. Therefore, it is essential to subject new materials and solutions to extensive testing to ensure their efficacy in preventing water leakage from precipitation.

Precipitation accompanied by wind, or simply wind-driven rain (WDR), pushes water to exposed façades as well as through leakages and cracks in the façades [12,13]. The amount of WDR impacting on a façade depends on wind velocity, rain intensity, size of rain droplets, building's geometry and surrounding [12,14,15]. When water droplets hit the façade, the wetting of the wall takes place due to capillary suction and infiltration through openings, such as cracks, connections to windows, attachment details, and fittings. Because designing and executing these parts with the required level of certainty can often be challenging, some

^{*} Corresponding author.

E-mail address: ali.karim@chalmers.se (A. Naman Karim).

<https://doi.org/10.1016/j.buildenv.2023.110905>

Received 5 July 2023; Received in revised form 12 September 2023; Accepted 4 October 2023

Available online 4 October 2023

0360-1323/© 2023 The Authors. Published by Elsevier Ltd. This is an open access article under the CC BY license (<http://creativecommons.org/licenses/by/4.0/>).

rainwater leakage should always be accounted for in hygrothermal (heat and moisture) simulations [16,17].

There are several standardized laboratory tests for assessing the watertightness of wall assemblies to rainwater [14]. Pass/fail criterion is normally used for these tests and up to a specified pressure difference. The watertightness tests are either dynamic tests, wind tunnel tests, or more commonly static, or cyclic tests. In all methods, a pressure difference is generated over the test wall to simulate wind. Rainwater is either directly sprayed onto the wall surface (standard EN 1027 [18]), or spread by a combination of water-spray and a water runoff film (standard EN 12865 [19]). In wind tunnel testing, water droplets are released into an air stream before reaching the wall surface.

In a static test [18], a constant water-spray intensity is maintained on the wall surface in combination with a constant overpressure (1200 Pa at maximum) for up to 15 min. In Europe, the recommended water intensity is 2.0 L/(min·m²) while 3.4 L/(min·m²) in North America [14]. For cyclic tests, the standard [19] specifies a 1.2 L/(min·m²) runoff intensity and a water-spray rate of 1.5 L/(min·m²) combined with a pulsating overpressure on the wall (minimum surface area: 1.2 × 2.4 m²). The tests continue until visible water penetration occurs on the interior side of the wall. The time, location of the water penetration, and air pressure difference at that moment are recorded. According to Ref. [19], the moisture absorption can be measured by comparing the mass of the test wall before and after testing.

The test conditions used in the aforementioned tests are sometimes regarded as extreme boundary conditions [14,20,21], more applicable to high-rise buildings. Moreover, peak rain intensities are more frequently accompanied by lower wind velocities [14]. Multiple studies [22–27] have thus taken into account the actual microclimate when designing the boundary conditions for WDR tests. Either low water spray rate and high pressure difference are recommended, or the opposite, as better choices than simultaneous peak rain intensities and wind velocities [14]. In Belgium and the Netherlands, this translates to test conditions of either 0.75 L/(min·m²) with up to 500 Pa pressure difference, or 2 L/(min·m²) with up to 150 Pa. For the Swedish climate, Kahangi Shahreza et al. [20,21] considered test conditions of 0.03–0.1 L/(min·m²) water spray rate, which is less than 7% of the values defined by the standards, combined with zero dynamic overpressure. These test conditions in Refs. [20,21] were selected to replicate the most frequent WDR events in four Swedish cities.

The inclusion of realistic boundary conditions in such tests, especially when evaluating new technical solutions, yields valuable insights into their moisture performance within specific microclimates. Furthermore, new solutions sometimes utilize unproven material combinations with distinct properties compared to conventionally tested materials. Therefore, a thorough assessment of their moisture absorption under rainwater wetting is required, going beyond a binary pass/fail criterion for watertightness, to ensure their long-term performance.

1.1. Aerogel-based coating mortars: response to rainwater

One of these new multifunctional solutions are the new energy-efficient coating systems with aerogel-based coating mortars (ACM-systems) [28]. In dry conditions, the declared thermal conductivity of ACMs is 30–50 mW/(m·K), which is less than 10% of that for conventional coating mortars. ACMs are composed of a blend of lime- and white cement-based binder, while, unlike conventional coating mortars, the sand in the mixture is replaced by hydrophobized silica-based aerogel granules [29–35] as aggregates. They also incorporate different additives such as air-entraining and water-repellent agents. Prior research has demonstrated that the utilization of 15–60 mm of ACM on uninsulated masonry walls led to a U-value reduction of 27–70% [28]. Due to their low mechanical strength, ACMs are reinforced by a mesh and covered on the outside by layers of ordinary mortars. ACM-systems fulfill the roles of a conventional coating mortar and a thermal insulating layer. Apart from their energy-saving potential, they can also

introduce new solutions to preserve the character-defining elements of façades when retrofitting culturally significant buildings.

Although extensive research has been conducted on the thermal performance of ACM-systems [36–45], less is known about their response to rainwater. Few studies [46–51] have investigated the response of ACMs to weathering in laboratory. Guzzardi [46] and Guzzardi et al. [47,48] conducted research on the hygrothermal performance of walls internally insulated with ACM, utilizing laboratory measurements and numerical hygrothermal simulations. The measurements in Refs. [47,48] were used to assess the test setup, and gathered experimental data to validate simulation models. Temperatures, relative humidities, and the arrival time of the waterfront were measured at various depths of a rendered brick masonry wall (1.8 × 1.5 m²) insulated internally with 60 mm of a commercial ACM. For four months, the exterior of the wall was exposed to cyclic loading, including 1 h of wetting (2 L/(m²·min)), 1 h of drying at room conditions and 4 h of irradiation to simulate artificial sunlight. In Ref. [46], it was concluded that internal application of ACM provides a moisture-safe retrofitting solution considering the potential risk of moisture accumulation and inadequate drying performance. However, this conclusion depends on the water absorption characteristics of the external wall [46]. In Ref. [49], Sakiyama et al. exposed a test wall (4.0 × 2.1 m²) insulated externally by 25 mm of a non-commercial ACM to weathering cycles including heating (up to 70 °C), cooling (down to –20 °C), and wetting (1.5 L/(m²·min)). The measurements revealed high water absorption in the analyzed coating system, resulting in damage caused by frost exposure during weathering cycles [49]. Therefore, it was concluded that the outer coating should be selected with care to control the water absorption. Maia et al. [50] assessed the capillary water absorption of non-commercial ACMs before and after subjecting them to consecutive laboratory weathering cycles involving wetting-drying, heating-freezing combined with infrared radiation. The results showed relatively high but stable water absorption of the ACMs before and after the weathering cycles. Karim et al. [51] measured the capillary water absorption of a commercial ACM exposed to three wetting rounds. Cubic samples of the ACM were soaked in water for 90 min, and subsequently dried. The measurements showed that the absorption by the ACM samples increased by up to 2.6 times during the third wetting round compared to the initial round. Correspondingly, the calculated capillary water absorption coefficients were more than five times higher. Possible reasons for this phenomenon may be attributed, among other factors, to alterations in the structural composition of the ACM or the aerogel granules caused by wetting and drying [51]. Although the studied ACM shall not be used as a standalone coating, its large change in water absorptivity may be of importance in moisture-safe design.

Up to this point, most experimental studies assumed undamaged ACM-systems. However, cracks, joints and other imperfections can allow rainwater to penetrate through the façade and damage the moisture-sensitive components of the walls. For ACMs, rainwater leakage can also reduce their thermal resistance. There are several origins for crack formations in coating mortars such as moisture and/or temperature induced stresses, mechanical impacts from wind or external forces [52–54].

The amount of water that penetrates through a crack depends on various factors, including the depth and width of the crack. Superficial cracks or scratches with shallow depth may be considered watertight, whereas continuous deep cracks wider than 0.3 mm will most likely result in rainwater penetration [55]. For other materials such as concrete, the water penetration through cracks narrower than 0.025 mm is negligible [56,57] but increases exponentially above this width [58–60]. Surface cracks commonly observed in coating mortars are either single or networked linear cracks [52]. They typically appear in areas with high stress concentration, including wall joints, corners, or around windows. To create relevant testing conditions, several methods have been used to introduce artificial cracks in coating mortars such as cyclic wetting-drying (swelling-shrinking), or application of external forces

[56,61,62]. However, these methods do not permit precise control over crack formation in terms of size, shape, and location, limiting the repeatability of experiments.

The presented literature review highlights a scarcity of research on the moisture absorption of externally applied ACM-systems during wetting. Additionally, previous studies have utilized rather extreme test conditions that do not accurately represent specific microclimates. Surface defects have also received relatively limited attention in prior works.

Therefore, this study aims to investigate the moisture absorption of a commercially available ACM-system under various wetting scenarios. It also examines the impact of water-repellent paint and surface cracks on moisture absorption and drying performance of the ACM-system. Furthermore, a newly developed tailor-made small-scale test setup (runoff setup) is introduced. This setup is specifically designed to replicate rainwater runoff caused by WDR on façades, based on historically prevalent WDR intensities in Swedish climates. Compared to existing standardized test methods for evaluating watertightness, this setup offers several advantages. These include increased efficiency and ease of use due to its small-scale nature, the ability to simulate low-intensity wetting scenarios, and real-time monitoring of both total moisture absorption and moisture distribution at different depths of the specimen during wetting and drying phases.

1.2. Overall methodology and layout

The investigation comprises a main and two complementary experimental studies (Fig. 1). The main study focuses on measurements in the runoff setup. Specimens of the ACM-system are subjected to wetting through water runoff and subsequently dried to their initial state. Moreover, the experimental results from the main study are compared to

simulated results from a simplified numerical model designed to simulate moisture transport within the ACM-system during wetting and subsequent drying. This comparison is done to explore the level of agreement between the two and to provide insights for future numerical studies and model refinement.

The complementary studies aim to explore additional wetting scenarios not covered in the runoff setup. The first study involves a capillary water absorption test at low/zero hydrostatic pressure (free suction), which involves soaking specimens in shallow water from one side. The water absorption of the specimens is then determined through three wetting rounds between which the samples are dried to initial mass. The second complementary study is also a suction experiment but at elevated hydrostatic pressure created by the Karsten tube. In these studies, specimens with and without water-repellent paint and surface cracks are prepared to assess their impact on the moisture absorption and drying performance of the ACM-system.

The paper is structured as follows: Chapter 2 presents the main study using the runoff setup. Chapter 3 describes the complementary studies. Chapters 4 and 5 present and discuss the findings, and Chapter 6 presents the conclusions.

2. Main study: runoff setup

The runoff setup (Figs. 1 and 2) was designed to replicate rainwater runoff on the specimen's exterior surface. The design idea of this configuration was influenced by established testing protocols in EN 1027 [18] and EN 12865 [19]. Comparable setups can also be observed in the works of others [20,21,63]. The runoff setup consisted of a cubic box with an interior volume of $1.4 \times 1.5 \times 0.75 \text{ m}^3$ (Height \times Width \times Depth). The exterior of the cube was covered with vapor-resistant plastic sheets (μ -value: $3 \cdot 10^5$), having a detachable front screen. The setup was

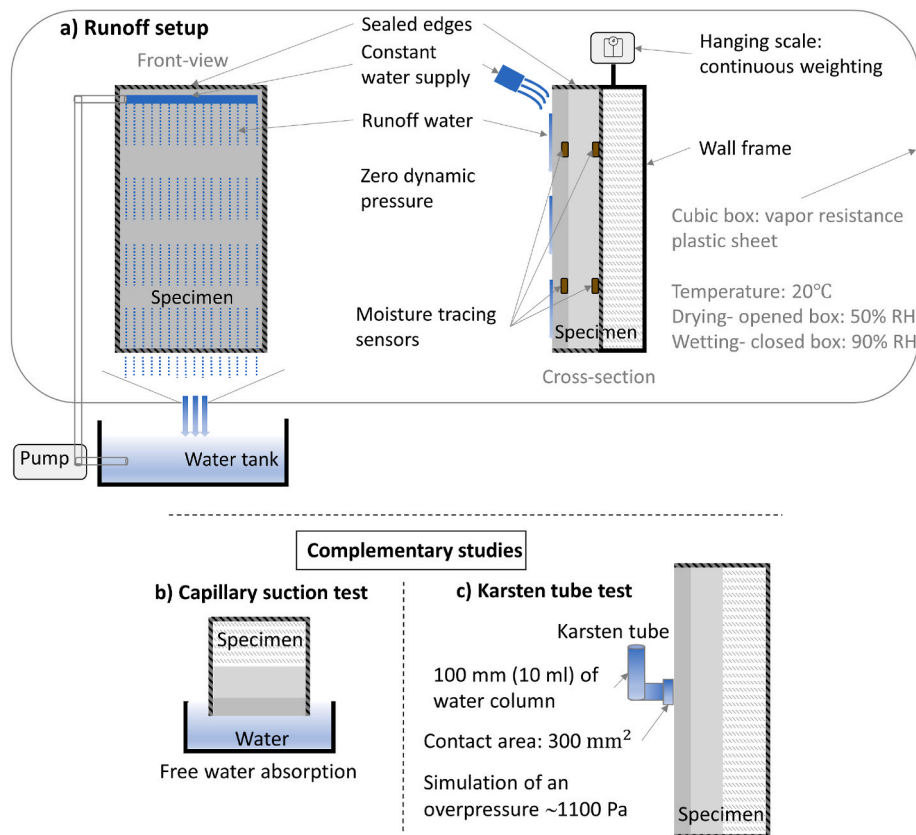


Fig. 1. Illustration of the experimental studies conducted. a) Main study using the runoff setup. Specimens are exposed to water runoff with zero overpressure applied on the surface. b) Capillary suction test where specimens are soaked in water from one side. c) Karsten tube test to measure the water absorptivity of the specimens when exposed to high overpressure.

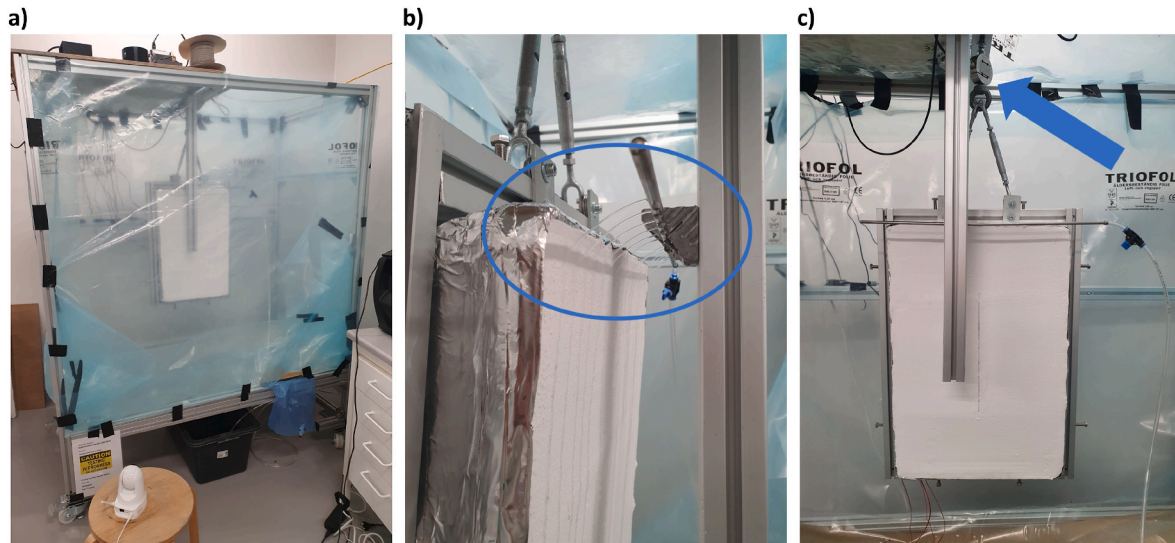


Fig. 2. a) Front-view of the setup during wetting (closed box: $90 \pm 5\%$ RH). The setup was placed in a climate-controlled room ($20 \pm 1^\circ\text{C}$, $50 \pm 2\%$ RH). At drying, the front was opened. b) Water supply pipe mounted in a fixed position in front of the test wall (indicated by blue oval). Continuous water flow was supplied through 15 identical circular openings with a 1 mm inner diameter. c) A specimen suspended from a hanging scale (blue arrow) for continuous weighing during wetting and drying. (For interpretation of the references to colour in this figure legend, the reader is referred to the Web version of this article.)

installed inside a climate-controlled room with constant climate of $20 \pm 1^\circ\text{C}$ and $50 \pm 2\%$ relative humidity (RH). During wetting, the box remained closed to maintain high humidity ($90 \pm 5\%$ RH). This was done to mimic high air humidity during rain and to restrict evaporation from the wet specimen surface. During drying, the front of the box was opened to allow drying towards 50% RH. The specimen, mounted in a metal frame (Height \times Width: $0.61 \times 0.41\text{ m}^2$, mass: 4.4 kg), was suspended from a hanging scale to monitor mass changes. A water system delivered a constant flow to simulate rainwater runoff, and moisture tracing sensors inside the specimen tracked RH changes. Further details about the specimens, runoff setup, and measurement scheme are provided in subsequent sections.

2.1. Undamaged specimens: ACM-system

The ACM-system specimens were prepared as illustrated in Fig. 3. The casting procedure, choice of mortars, application sequence, and curing times adhered to the manufacturer's instructions. To isolate the experiment from substrate impact, all sides of the aerated concrete

substrate were sealed with epoxy glue. The ACM-system was cast by first applying an undercoat mortar to the fully sealed substrate, followed by the ACM. The undercoat served to strengthen the adhesiveness between the ACM and the substrate. The applied ACM layer was approximately 40 mm thick, as per standard practice [28]. After curing for 28 days, a primer was applied followed by the first layer of outer coating mortar reinforced with a glass fiber mesh. The second layer of outer mortar was added after curing. These layers provided the ACM-system the necessary mechanical strength. Some specimens had a water-repellent paint applied in three steps: primer and two coats of paint, following the technical data sheet (TDS) [64]. The preparation time for a single specimen including curing time for all layers was approximately 50 days. All sides of the specimens were sealed to restrict all moisture flux exchange with the surroundings to the exterior surface alone. This would represent an extreme case of unidirectional moisture transport through the exterior, where interior drying is prevented.

Table 1 presents the material properties of the principal layers of the ACM-system, as declared in their respective TDS [64]. The Specific product types for the components in the mixture, including the aerogel

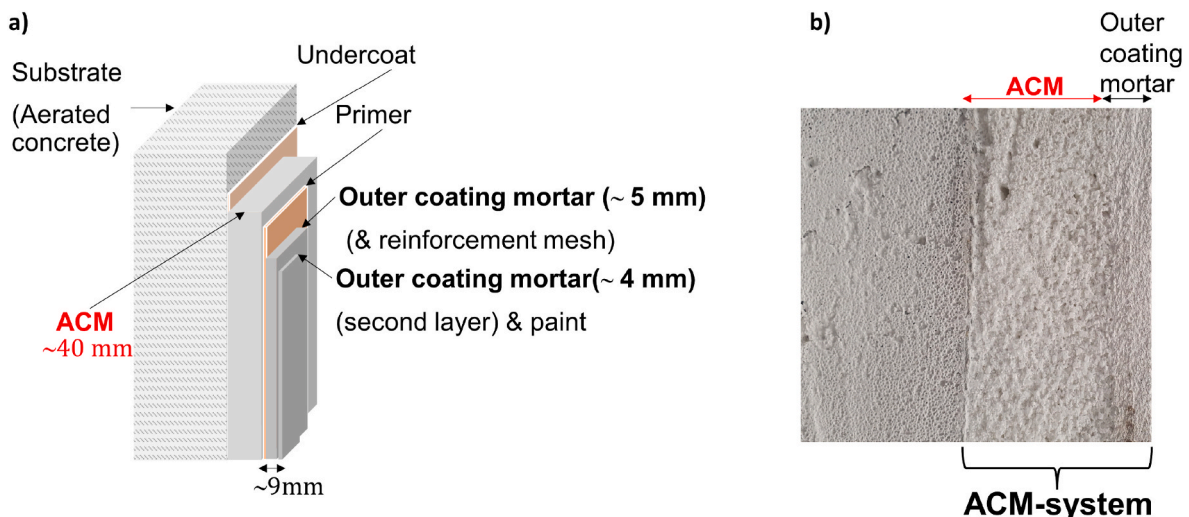


Fig. 3. a) Schematic of the ACM-system. b) Cross-section of a cast specimen with the main layers highlighted.

Table 1
Declared material properties [64] of the principal layers in the ACM-system.

Material property	ACM	Outer coating mortar	Water-repellent paint
Density, ρ (kg/m ³)	180	1200	–
Thermal conductivity, λ_{dry} (mW/(m·K))	40	930	–
Water vapor permeability coefficient, μ -value (–)	≤ 5	10	(s_d -value ^b = 0.01 m)
Water absorption coefficient, A_{cap} (kg/(m ² ·min ^{0.5}))	≤ 0.2	≤ 0.4	0.01–0.06
Compressive strength, σ_c (N/mm ²)	0.5	1.3	–
Moisture dependent thermal conductivity ^a , $\lambda(RH)$ (mW/(m·K))	RH (%)	$\lambda(RH)$	–
	0	40	–
	80	45	–
	90	50	–
	100	400	–

^a Measured in the laboratory (ISO 22007-2 [65]).

^b A s_d -value of 0.01 m corresponds to a vapor resistance of 0.01-m-thick layer of stagnant air.

granules, are not disclosed by the manufacturer. The ACM and outer mortar contained hydrophobic agents to enhance water-repellency [64]. In Fig. 4, the four types of specimens (0.6×0.4 m²) are depicted. For consistency and clarity, the study will refer to the four specimen types as Façades I–IV. Façades I–II represent undamaged specimens (Fig. 3). While Façade II was externally coated with water-repellent paint, Façade I had an unpainted outer coating mortar, serving as the reference case. The damaged specimens, Façades III–IV, featured a horizontal and vertical surface crack, respectively (Section 2.2 provides further details). Like Façade II, Façades III–IV were externally painted.

2.2. Specimens with surface damage: artificial vertical and horizontal cracks

Façades III–IV were included in the study to evaluate the influence of surface cracks on the wetting and drying of the ACM-system. Fig. 5, demonstrates the production of cracks by inserting a 0.3 mm thick metal sheet into both layers of the outer mortar during the fresh stage. Due to the fragility of the ACM, mechanical impact on the hardened mortar could lead to breakage or non-identical cracks. The final cracks were around 9 mm deep, protruding through the entire outer coating to the front side of the ACM. At the hardened stage, the cracks had an average width of 1 ± 0.5 mm and a length of 300 mm, centered on the surface.

2.3. Water supply system

A micropump (MGD1000 model) provided a steady and pulsation-free water supply to a water distributor (Fig. 1), wherefrom the water ran over and off the specimen surface. The pump, operated by a separate brushless motor controller, sourced water from a 60-liter tank positioned beneath the setup. The water supply rate was set to 2 L/(m²·min), resembling the runoff on a wind-ward façade created by the most frequent WDR intensities in Swedish climates (see Appendix A). The water distributor was a stainless-steel pipe fixed at 70 mm distance from the specimen and aligned with its top edge (Fig. 2 middle), featured 15 circular openings. These openings had a 1 mm inner diameter and were spaced 25 mm apart. Relatively stable meanders from these openings at the top simulated rainwater runoff on the surface. Importantly, these dynamic rivulets were permitted to flow freely across the surface, leading to eventual surface saturation and the formation of a water film. The resulting runoff water was collected in the tank via a hole at the bottom of the setup and recirculated back to the distributor.

2.4. Monitoring system: weighing scale

A hanging scale (OIML C2.S) with a maximum capacity of 50 kg

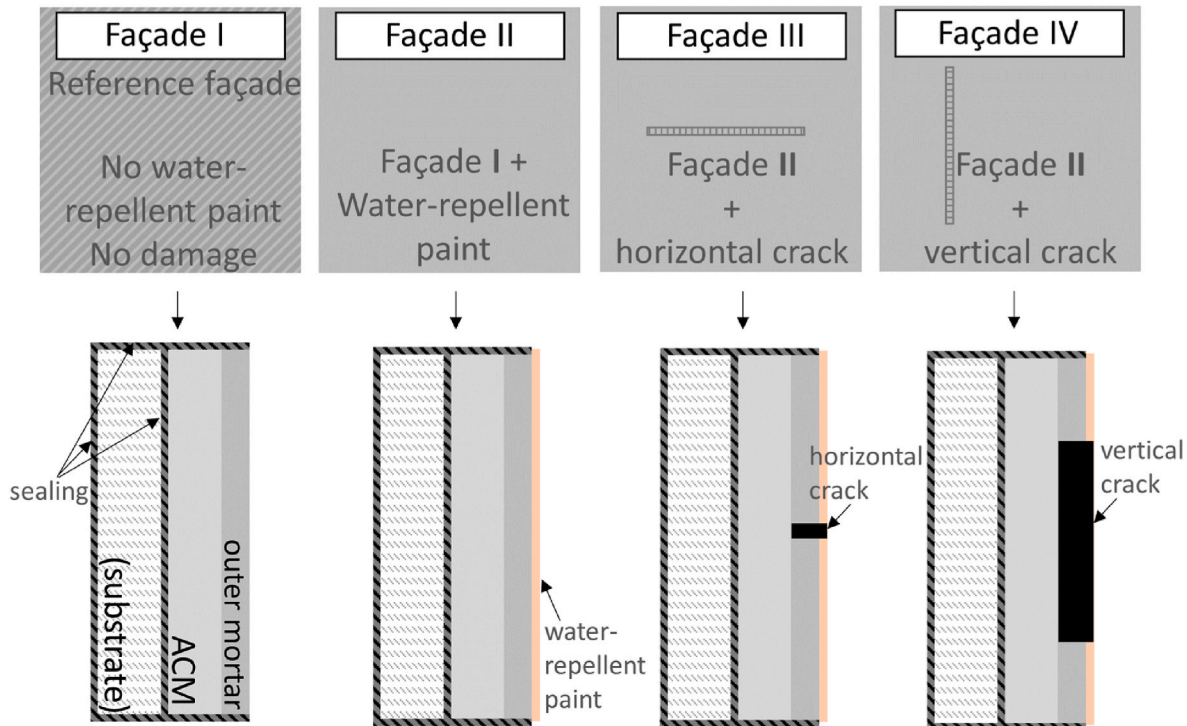


Fig. 4. Four specimen types used in the measurements. Unlike Façade I, Façades II–IV were externally covered with water-repellent paint. Façades III–IV included a horizontal and vertical crack, respectively.

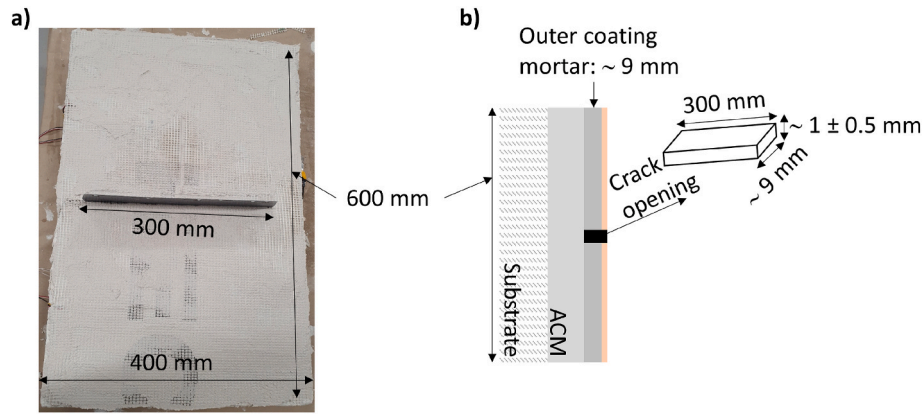


Fig. 5. Creation of surface defects in Façades III-IV. A metal sheet was inserted through both layers of outer mortar (fresh mortars) to produce a vertical (Façade IV: Fig. 2c) or horizontal crack (Façade III). a) A sheet penetrating the first layer of outer mortar and mesh for a horizontal crack. b) Schematic on the dimension of the final crack opening at hardened stage (crack width: 1 ± 0.5 mm, crack depth: 9 mm, crack length: 300 mm).

monitored the mass change of the specimens (Fig. 2c). The registered mass change included both the moisture absorbed by the specimens and the water runoff on the surface. The scale had a declared sensitivity of 2 mV/V and a mechanical accuracy of ± 0.025 kg. A real-time controller operated the scale, collecting and logging the average of 1000 measurement points per minute. The weighing system was calibrated for a measuring range of 0–25 kg, with a maximum error of 1%. For the mass change interval relevant to the measurements conducted, the error of the weighing system was below 0.01 kg.

2.5. Monitoring system: moisture tracing sensors

To track RH changes in the specimen, two moisture tracing sensors were positioned in the outer coating mortar and two others in the ACM, at depths of around 9 mm and 49 mm from the exterior surface, respectively. Vertically, the sensors were placed in the center of the upper and lower halves of the specimens, as shown in Fig. 6.

The sensors used were capacitive moisture sensors with two isolated thin copper electrodes, encased in corrosion-resistant sheeting to prevent water contact and corrosion. The two electrodes function as a variable capacitor whose capacitance changes with humidity in the surrounding. Each sensor comprises an electrical module with a built-in timer chip (TLC555C), sealed with protective lacquer before

installation. The timer measures the charging and discharging time of the capacitor, which is converted into proportional analog output voltage. This value can be read by an analog to digital converter (ADC) and subsequently interpreted as the humidity of the medium in contact with the sensor. The sensors were read using a microcontroller unit (MCU) (NodeMCU ESP8266 model) with an integrated ADC (10-bits) and Wi-Fi chip. The MCU collected data from each sensor every 20 s, transmitting online readings. Prior to the experiment, the system was calibrated in a climate-controlled chamber at a constant temperature of 20 °C and at RHs of 50%, 70%, 85%, 95%, and wet condition (100% RH).

2.6. Measurement scheme

Table 2 presents the measurement scheme for the runoff setup. Each test (Façades I-IV) involved two identical specimens (specimens 1 and 2) to measure the repeatability of the results. Each specimen was wet and dried three times. The wetting phase lasted 24 h, aimed at simulating an extreme case of prolonged rain event. Because the drying of specimens was time demanding, it was split in two phases. The first 144 h (6 days) of drying was conducted in the runoff setup with the sample hanging on the scale and the plastic chamber opened on one side. Thereafter, the sample was placed elsewhere in the climate room and dried naturally to

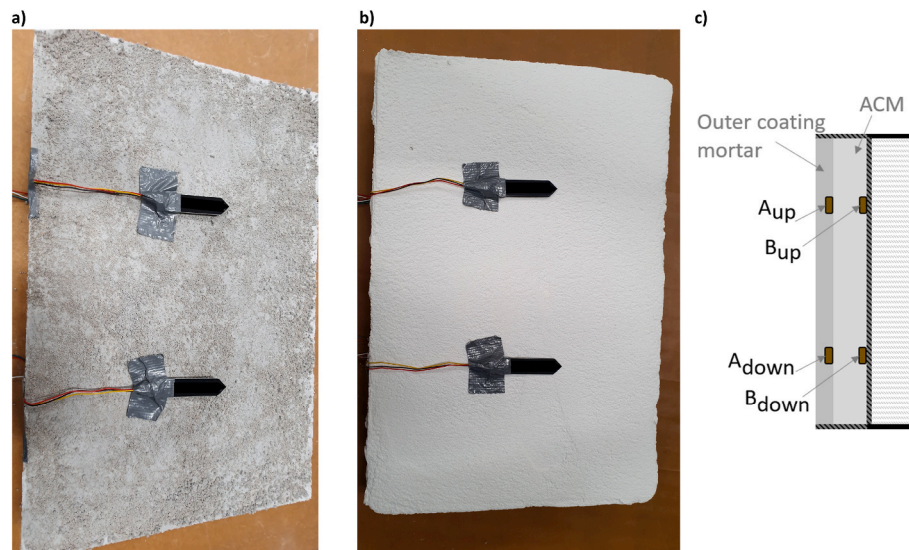


Fig. 6. Moisture tracing sensors positioned at the center of the vertical upper and lower half of the specimen during casting. a) Behind the ACM (B_{up} , B_{down}). b) Behind the outer mortar (A_{up} , A_{down}). c) Schematic of the sensor positionings.

Table 2
Measurement scheme for the runoff setup.

Runoff setup	Façade I	Façade II	Façade III	Façade IV
Surface quality	No water repellent paint, no damage	Water repellent paint, no damage	Water repellent paint, one horizontal crack	Water repellent paint, one vertical crack
Number of specimens	2	2	2	2
Number of wetting and drying rounds	3	3	3	3
Duration of wetting phase	24 h	24 h	24 h	24 h
Duration of drying phase in the setup ^a	144 h	144 h	144 h	144 h

^a The remaining time until complete drying back to initial state was spent outside the setup in the same climate room (20 °C, 50% RH).

its initial mass. The average time between two consecutive wetting for the same specimen exceeded 60 days.

2.7. Numerical hygrothermal simulations

For the purpose of future numerical studies, a numerical hygrothermal model of the reference specimen, Façade I, was developed and verified by the measurements from the runoff setup in terms of total moisture content of the specimen and RH inside the outer mortar and the ACM. The model describes a dynamic one-dimensional moisture transfer through (porous) materials and is developed in COMSOL Multiphysics 6.0 by utilizing the physics module *Moisture Transport in Building Materials*. The governing balance equation for combined vapor and liquid transports in materials reads:

$$\xi \frac{\partial RH}{\partial t} + \nabla \cdot (-\xi D_w \nabla RH - \delta_p (\nabla RH p_{sat})) = G \quad (1)$$

Where ξ (kg/m³) is moisture capacity, RH (–) is relative humidity, D_w (kg/(m²·s)) is liquid transport coefficient (m²/s), δ_p (kg/(m·s·Pa)) is water vapor permeability, p_{sat} (Pa) is saturation vapor pressure, and G (kg/m³) is moisture source.

In the model, the conditions used in the runoff measurements were implemented. At surface boundary, RH (vapor concentrations at specified RH levels) was used as driving potential in the simulations to characterize the moisture transport. During the 24-h wetting phase, the front surface of the specimen was assumed to be wet (~100% RH), while the remaining surfaces were assumed to be sealed. The simulations were performed under isothermal conditions (20 °C), neglecting latent heat transport. The built-in COMSOL package for mesh generation was used, utilizing unstructured grids of triangular elements. A physically controlled mesh (extremely fine) and a 60-s time step were used. Table 3 presents the input data used in the simulations. Due to insufficient data, no hysteresis effects were considered in the sorption isotherm curves and thus the same parameters were used at wetting and drying phases. Similarly, the values of D_w were calculated using the simplified expression shown in Equation (2) [16], where A_{cap} (kg/(m²·s^{0.5})) is the capillary water absorption coefficient, w (kg/m³) is the moisture content, w_{sat} (kg/m³) is the free water saturation of the considered material.

$$D_w = 3.8 \cdot \left(\frac{A_{cap}}{w_{sat}} \right)^2 \cdot 1000 \frac{w}{w_{sat}-1} \quad (2)$$

Table 3
Input data used in the simulations.

Material property	ACM		Outer coating mortar	
Vapor permeability ^a , μ -value (–)	3		10 ^d	
Water absorption coefficient ^b , A_{cap} (kg/(m ² ·min ^{0.5}))	0.04		0.08	
Sorption isotherm-adsorption ^c , w (kg/m ³)	RH (%)	w	RH (%)	w
	0	0	0	0
	9	0.70	9	2.39
	33	1.64	33	4.57
	50	4.94	50	18.90
	75	9.32	75	39.40
	85	10.10	85	47.70
	93	18.30	93	53.10
	w_{sat}	484	w_{sat}	270

Measured in laboratory.

^a EN 1015-19 [66].

^b EN 1015-18 [67].

^c EN 12571 [68].

^d Declared value [64].

3. Complementary studies

3.1. Capillary water suction

The capillary water absorption of the ACM-system was measured according to EN 1015-18 [67]. Note that the standard prescribes measurement on a single material, whereas the presented measurements consider multiple materials. The tested ACM-system was the same as in the runoff tests (Fig. 3, Table 1) but of different size and substrate. The exposed or front sides of the specimens were 100 × 100 mm² (Fig. 7) and 20 mm thick plywood were used as substrates. Before the application of the ACM-system, all sides of the substrate were sealed with epoxy glue to eliminate its impact on the moisture transfer within the ACM-system. Prior to testing, all samples were preconditioned for approximately two months at 20 °C and 50% RH.

The measurement scheme comprised three tests (Façade I-III/IV) and nine measurements each (3 identical specimens × 3 wetting) as summarized in Table 4. The front side of the specimen was soaked in water (5–10 mm). Each specimen was placed in a closed container to minimize evaporation. Mass gain (kg/m²) was recorded after 10, 20, 45, and 90 min, as well as after 24 h using a weighing scale (METTLER TOLEDO PG503) with a resolution of 10^{−6} kg. The one test on Façade III/IV included damaged specimens, comprising a 30 mm long, 1 ± 0.5 mm wide and 9 mm deep crack on the front surface. While the cracks were placed centrally on the surface, their orientation when submersed in water was irrelevant.

3.2. Karsten tube measurement

The second complementary study involved the Karsten tube method, which currently lacks established standards apart from recommendations found in literature [69–71]. The Karsten tube, which consists of a dome with a diameter of 30 mm and a cylindrical tube with a volume of 10 ml (100 mm head of water), was affixed to the front surface of the specimen (Fig. 8). This created a hydrostatic pressure of approximately 1100 Pa, mimicking wind pressure at around 43 m/s wind velocity. The absorbed water was derived manually by monitoring the decreasing volume in the tube at intervals of 1, 5, 10, 15, 30, 60, and 90 min from the start of wetting. Once the volume decreased by 1 ml, it was refilled to maintain a constant pressure. Due to the small contact surface area of the dome, the wetting phase was limited to 90 min. An extended period of wetting would result in water being absorbed by the material surrounding the dome due to capillary forces, stretching the wetting area to an undefined shape and outside the applied pressure.

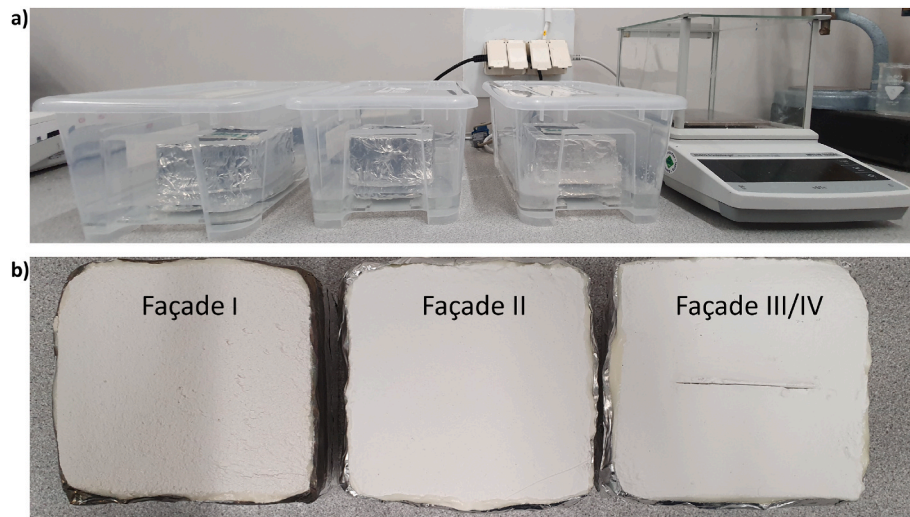


Fig. 7. a) Measurement setup used for the capillary water suction tests. The front sides of the specimens were soaked in 5–10 mm of water. All other sides were sealed. b) The side of the specimens immersed in water was $100 \times 100 \text{ mm}^2$.

Table 4
Measurement scheme for capillary suction tests.

Capillary water suction	Façade I	Façade II	Façade III/IV ^a
Surface quality	No water repellent paint, no damage	Water repellent paint, no damage	Water repellent paint, one crack
Number of specimens	3	3	3
Number of wetting and drying rounds	3	3	3
Duration of wetting phase	24 h	24 h	24 h

^a In these measurements, the orientation of the crack (vertical or horizontal) was irrelevant. Thus, only one type of damaged specimen (Façade III/IV) was considered.

Table 5
Measurement scheme for the Karsten tube tests.

Karsten tube method	Façade I	Façade II
Surface quality	No water repellent paint, no damage	Water repellent paint, no damage
Number of specimens	1	1
Number of wetting rounds	6	6
Duration of wetting phase	1.5 h	1.5 h

water through the crack opening. One specimen ($0.6 \times 0.4 \text{ m}^2$) was prepared for each façade as described in Fig. 3 and Table 1. For each specimen, six measurements were conducted.

4. Results

The results of the main study using the runoff setup are presented in Section 4.1. Section 4.2 presents the findings of the complementary studies while Section 4.3 compiles a comparison between the results of the main and complementary studies.

4.1. Runoff setup

In Fig. 9a, the mass changes (kg/m^2) of Façades I–II during 24 h of wetting and the initial 144 h of drying in the setup are presented. Both Façades I–II exhibited similar performance at wetting and drying. During the first 10 h of wetting, Façade II had up to 6% (0.04 kg/m^2) lower average mass gain, indicating a potentially higher runoff rate compared to Façade I. In contrast, after 24 h of wetting, Façade II had 9% (0.06 kg/m^2) higher average mass gain, suggesting increased runoff for Façade I as the outermost layer became saturated. During the initial 144 h of drying, approximately 85% (0.52 kg/m^2) of the total moisture absorbed by Façades I–II dried out. The average drying rate differed by about 2% between the two façades during this drying phase.

Fig. 9b illustrates the relative mass gain in percentage $((V_3 - V_1) \cdot 100 / V_1)$ during the second or third round of wetting (V_3) compared to the first round (V_1) for each specimen. For one specimen of Façade II (II-2) and both of Façade I, the mass gain during the second and third round of wetting increased by 10–16%, with a smaller increase observed between the second and third rounds. In contrast, for Façade II-1, the mass gain decreased by approximately 20% during the second and third rounds of wetting compared to the first round.



Fig. 8. Karsten tube affixed to the surface of a specimen. A steady water pressure created by 100 mm column corresponds to a wind pressure (1100 Pa) at velocity of 43 m/s.

Table 5 provides the measurement details. Only undamaged specimens (Façades I–II) were examined as applying the hydrostatic pressure on a crack was deemed unsuitable due to an immediate absorption of

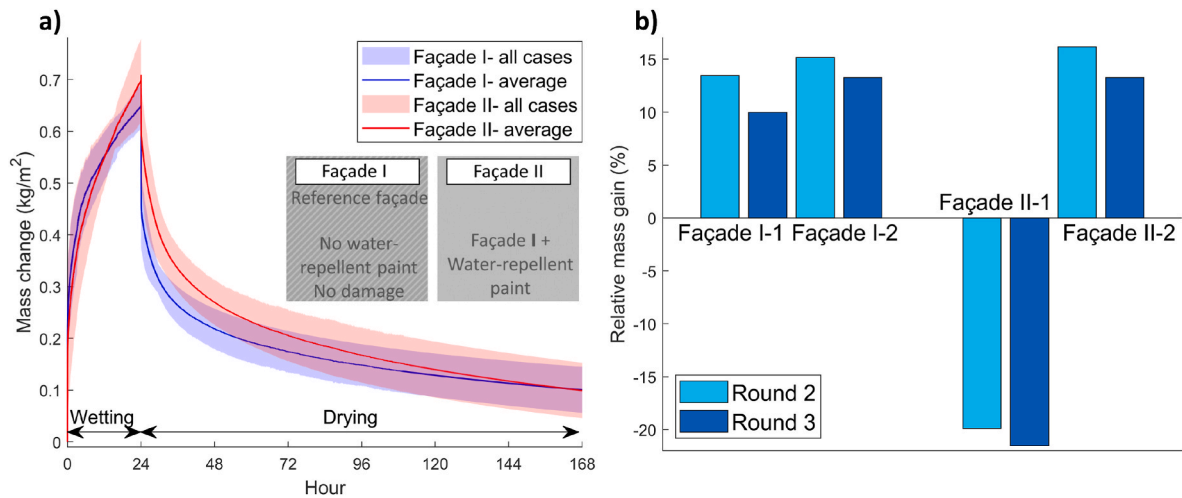


Fig. 9. a) Mass change (kg/m^2) of Façades I-II in the runoff setup. The Shaded graphs represent the total variability in all six rounds of measurements (2 specimens x 3 rounds) for Façades I-II. b) Relative mass gain during the second and third rounds of wetting relative to the first round.

Fig. 10 shows the RH measurements in Façades I-II. Both façades exhibit similar RH trends. The RH at position A_{up} and A_{down} , behind the outer coating mortar, peaked at 96% during wetting and fell to a minimum of 54% during the initial 144 h of drying. Behind the ACM, B_{up} , the highest average RH was 65% for Façade I and 62% for Façade II, 6 and 4 h after the end of wetting, respectively. At B_{down} , the highest average RH in Façade I was 59% at the end of wetting, while Façade II

recorded a maximum average of 64%, 5 h after the end of wetting. The increasing RHs behind the ACM after the end of wetting suggest moisture redistribution within the ACM towards the interior (substrate). After 144 h of drying, the RHs at B_{up} and B_{down} were reduced to around 52% for both Façades I-II.

Fig. 11 shows the mass change (kg/m^2) of Façades III-IV, which contained vertical and horizontal crack, respectively. As shown, the

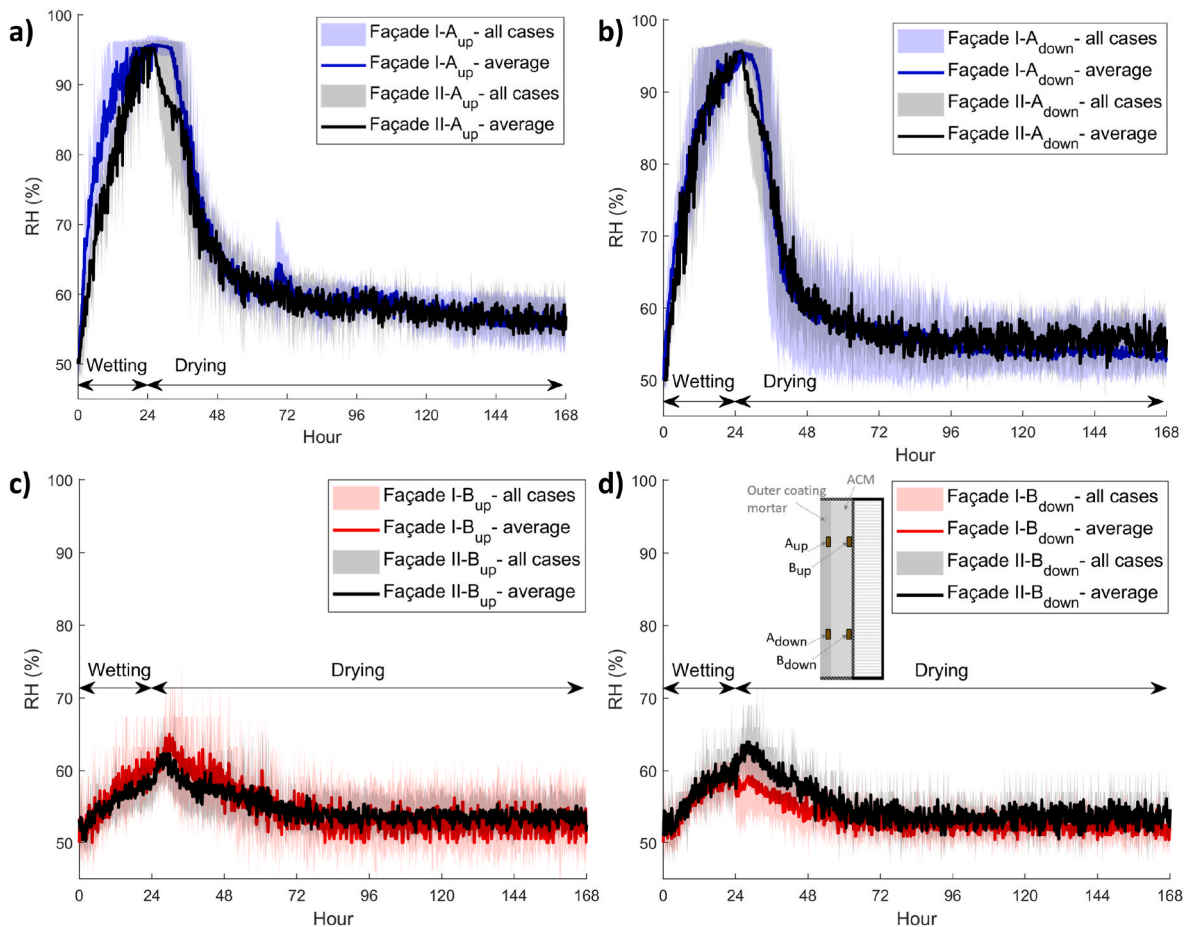


Fig. 10. Measured RH in Façades I-II in the runoff setup. The Shaded graphs represent the total variability in all six rounds of measurements (2 specimens x 3 rounds) for each façade.

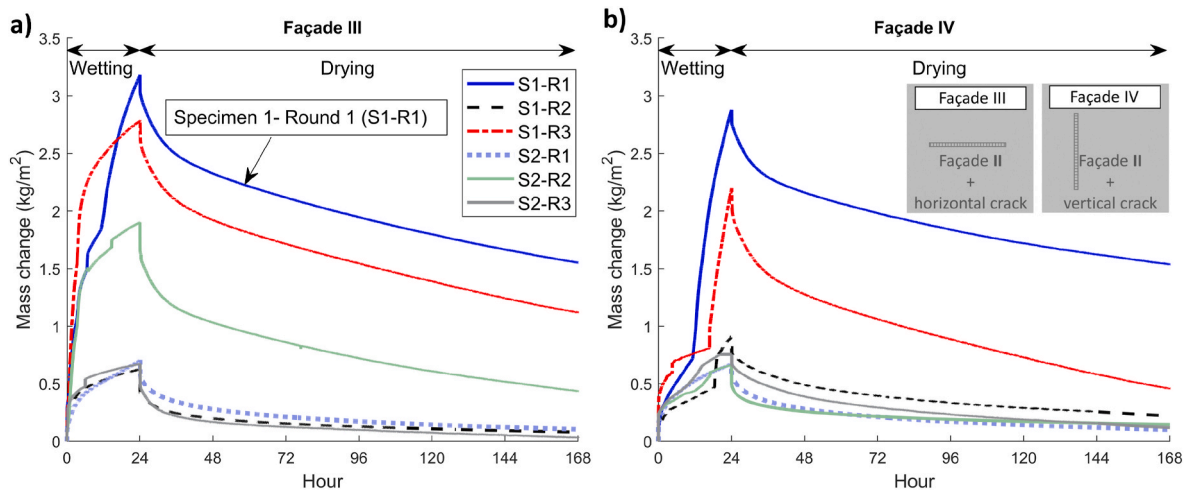


Fig. 11. Mass change (kg/m^2) in all six rounds of measurements (2 specimens \times 3 rounds) for Façade III (a) and IV (b) in the runoff setup. For reference, the maximum mass gain for Façades I-II was $0.6\text{--}0.7 \text{ kg/m}^2$.

response of the Façades to identical runoff wetting was scattered. For three respectively four out of six measurement rounds, the mass gain of Façades III-IV ($0.6\text{--}0.9 \text{ kg/m}^2$) was comparable to that of undamaged Façades I-II ($0.6\text{--}0.7 \text{ kg/m}^2$), indicating a less significant water penetration through the cracks. During the initial 144 h of drying, around 85–95% of the absorbed moisture was removed. However, for the remaining three respectively two measurement rounds of damaged Façades III-IV, the mass gain ($1.9\text{--}3.2 \text{ kg/m}^2$) was around 3–5 times

greater than for undamaged Façades I-II. As shown in Fig. 11, sudden increases in the mass change rates were observed in these measurement rounds after 5–20 h of wetting. For these rounds, approximately 50–65% of the absorbed moisture was removed during 144 h of drying.

To illustrate the highest RHs observed in the damaged Façades III-IV, Fig. 12 presents the measured RHs from the measurement rounds with the greatest water mass gain (S1-R1 in Fig. 11). Behind the outer mortar (A_{up} and A_{down}), the RH reached approximately 95–100% within the

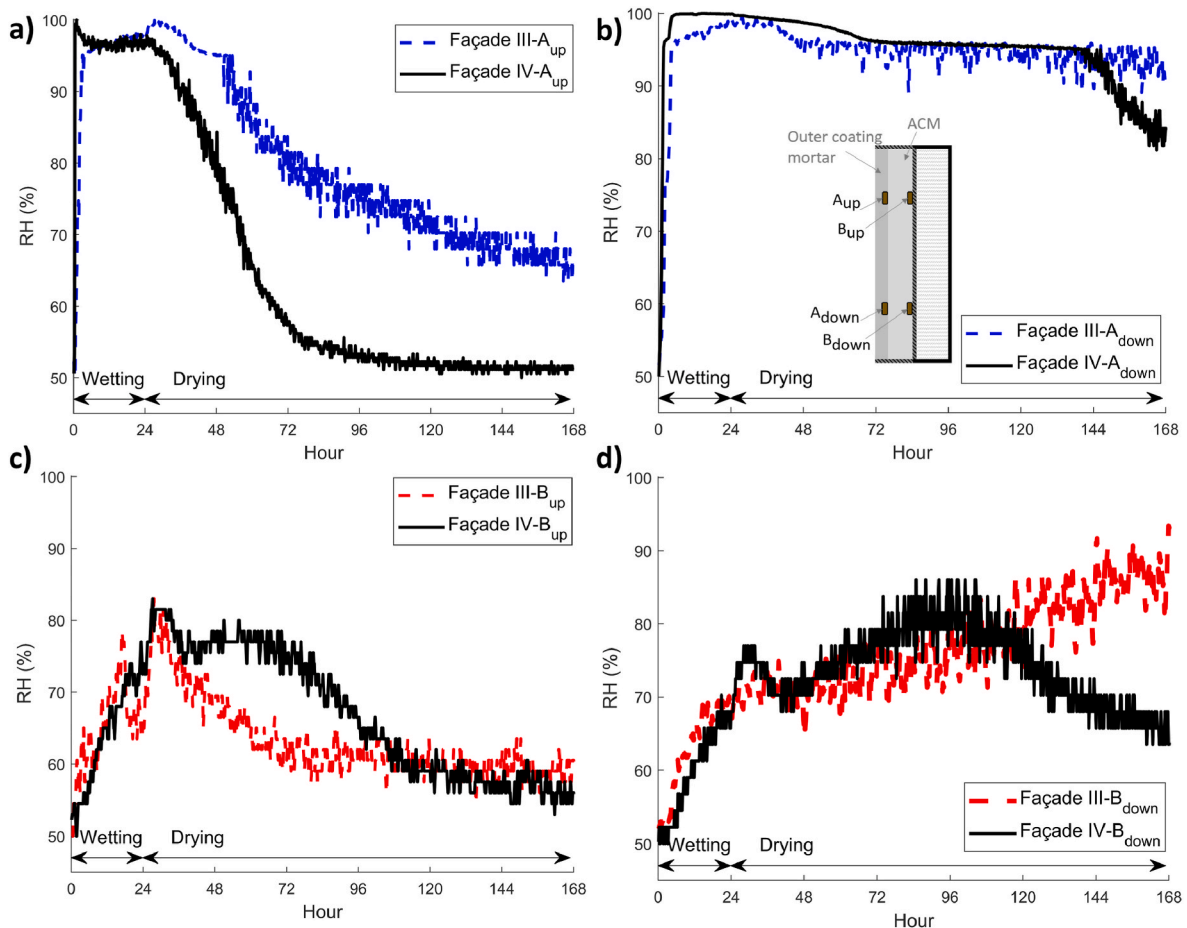


Fig. 12. Measured RH in Façades III-IV with the highest water absorption during wetting (Fig. 11: S1-R1) in the runoff setup.

first hour of wetting for both Façades III-IV. While the RH decreased at A_{up} during drying, the RH at A_{down} remained consistently high (above 95%) during the first 120 h of drying, indicating gravity-driven moisture redistribution from the upper to lower parts of the specimens. Similar trends were observed for the RHs behind the ACM, with a decrease at B_{up} and an increase at B_{down} during the initial drying phase. Behind the ACM, the RHs increased to approximately 85–95% before gradually declining towards 50% RH. It is important to note that this study only allowed for drying via the exterior surface, representing an extreme scenario.

Fig. 13 presents the simulation results of the wetting and drying of Façade I compared to the experimental data (Figs. 9 and 10). The simulations predicted on average 11% lower mass increase during wetting (Fig. 13a) than the experimental data. Notably, the simulations did not account for the mass increase from runoff water film formation on the surface. Furthermore, the surface boundary was assumed to be wet (~100% RH) during wetting, which is not fully representing the capillary liquid suction taking place on the surface boundary. During drying, the predicted values fell within the lower measurement variability range, with an error of up to 25% compared to average measurement values. The simulated RHs behind the outer mortar (Fig. 13b) were underestimated by up to 14% during wetting, while during drying, the simulated values had an error of up to 7%. For the RHs behind the ACM (Fig. 13c), there was a time shift of approximately 5 h between simulated and measured peak RHs, with an error of 1.5% in magnitude. The corresponding error at the end of 144 h of drying was around 8%.

4.2. Complementary studies

Fig. 14 illustrates the outcome of the three rounds of capillary suction tests at both 90 and 1440 min (24 h) of wetting, along with the corresponding standard deviation (SD). The 90 min wetting was selected according to the standard [67] and to give references for comparisons with the results from the Karsten tube tests. Similarly, the 24-h wetting was selected to give references for comparisons with the results from the runoff tests.

As shown in Fig. 14a, Façade II exhibited the lowest mass gain, while damaged Façade III had the highest gain at both 90 min and 24 h of wetting. After 24 h, Façade II absorbed around 50% less water than Façade I. Meanwhile, Façade III absorbed approximately 13% more than Façade I. In Fig. 14b and c, the relative mass gain during the second and third rounds of wetting compared to the first round is shown for Façades I-III. The highest relative change between measurement rounds was less than 7% at 90 min and less than 13% at 24 h. The coefficient of variance (CV) for the capillary suction tests was within 10–23% for Façade I, 7–25% for Façade II, and 3–28% for Façade III.

The findings of the Karsten tube test for Façades I-II are displayed in Fig. 15. Façade II consistently exhibited lower water absorption compared to Façade I. After 5 and 90 min of wetting, Façade II absorbed approximately 75% and 51% less water than Façade I, respectively. The former scenario could represent the water absorption during a brief WDR event lasting only a few minutes. The CV for the measurements on Façades I-II was between 10–31% and 15–22%, respectively.

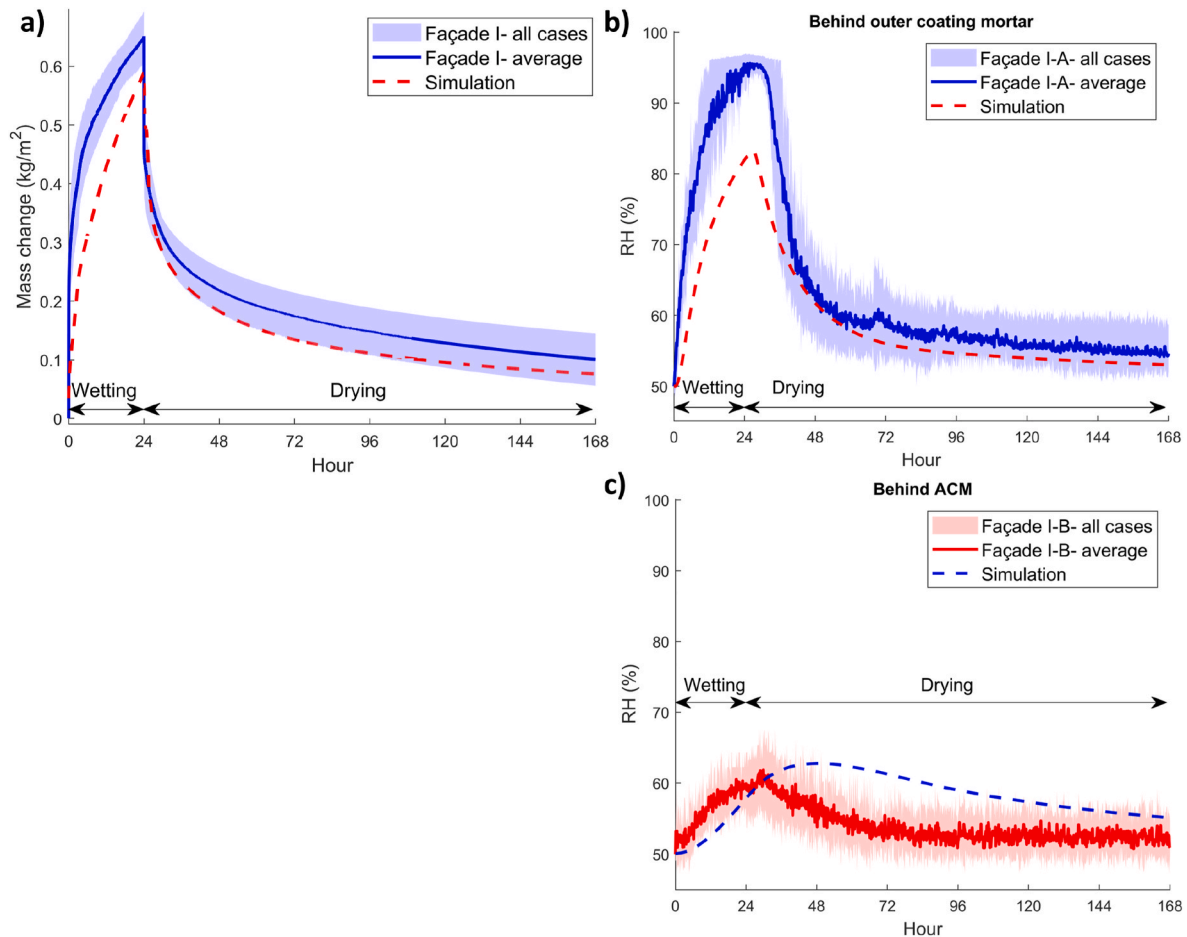


Fig. 13. Comparison between the simulated results and the measurements for Façade I in the runoff setup. a) Mass change. b) RH behind the outer mortar (average of A_{up} and A_{down}). c) RH behind the ACM (average of B_{up} and B_{down}).

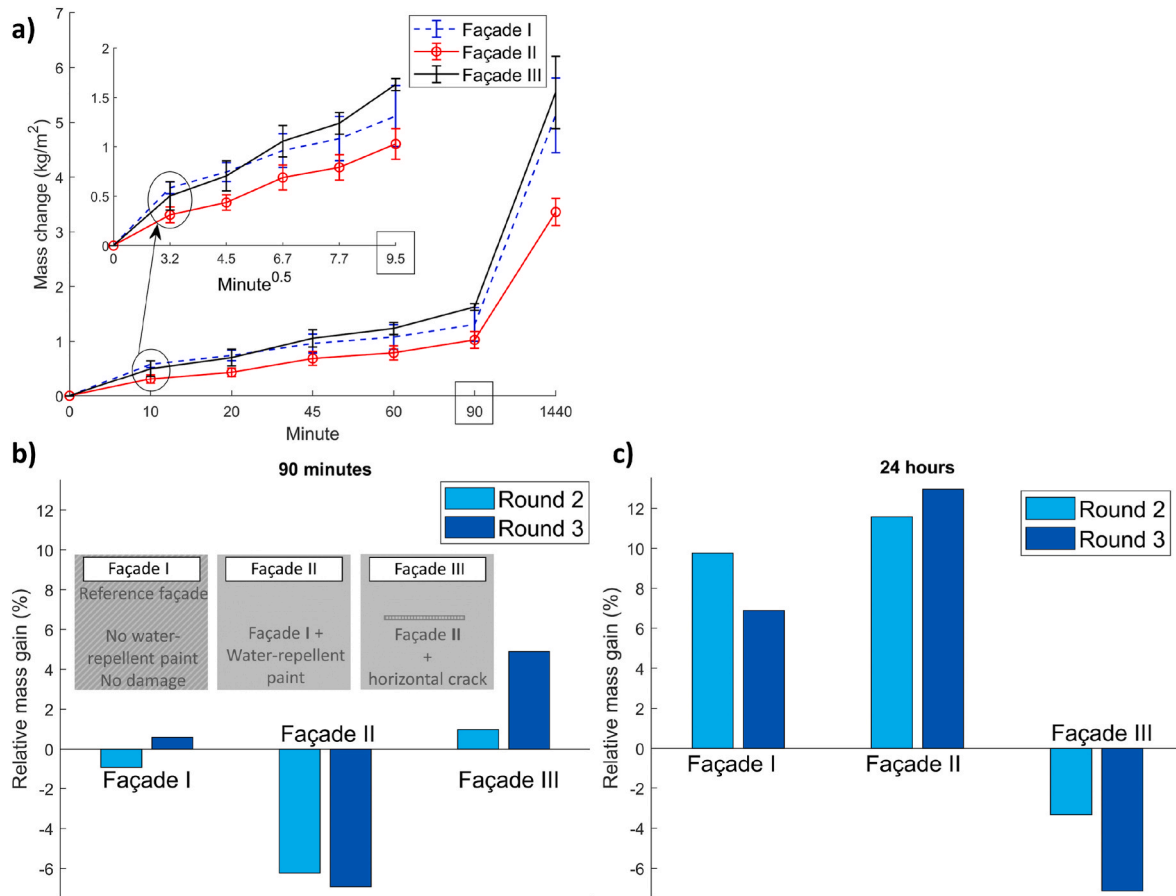


Fig. 14. a) Average capillary water suction (kg/m^2) and the corresponding SD of the three measurement rounds for Façades I-III for 90 and 1440 min (24 h). Using an x-axis of $\text{minute}^{0.5}$ ($90 \text{ min} \rightarrow 9.5 \text{ minute}^{0.5}$), the embedded plot depicts the water suction during the first 90 min. b, c) Relative mass gain at the second and third round of 90 (b) and 1440 (c) minutes wetting relative to the first round.

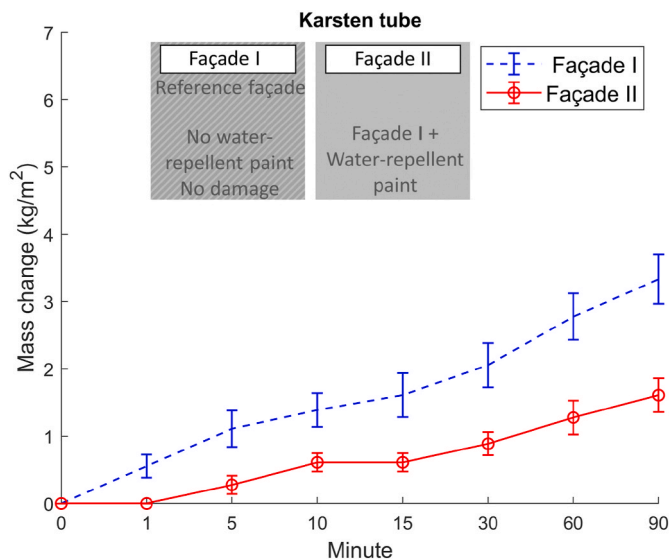


Fig. 15. Water absorption for the Karsten tube test for 90 min.

4.3. Comparison of moisture absorption for the three wetting scenarios

Fig. 16 presents a comparative analysis of the maximum moisture absorption of Façades I-IV for the three wetting scenarios, i.e. runoff, capillary suction, and the Karsten tube. The results are presented for

short-term (represented by 90 min) and long-term (24 h) wetting. For each wetting scenario, the absolute mass change (kg/m^2) and the relative mass gain (%) of Façades II-IV compared to Façade I (reference case) are provided. To be noted is the difference between the crack length of the damaged façades used in the runoff setup (crack length: 300 mm, wall surface: $600 \times 400 \text{ mm}^2$, ratio: 5/10 or 7.5/10) and those used in the capillary suction test (crack length: 30 mm, wall surface: $100 \times 100 \text{ mm}^2$, ratio: 3/10).

For the wetting scenarios examined, runoff wetting resulted in the lowest water absorption for all Façades. Façade III had the highest mass gain, approximately 1.0 kg/m^2 at 90 min and 3.2 kg/m^2 at 24 h of runoff wetting. In contrast, Façade I had values of 0.4 kg/m^2 and 0.6 kg/m^2 for the same time intervals, respectively. Façade II, with water-repellent paint, showed 15% lower mass change than Façade I for short-term wetting and 9% higher mass change for long-term wetting. Among Façades III-IV, Façade III with a horizontal crack had the maximum mass increase.

In the capillary suction test, Façade II had the lowest mass increase, while the damaged Façade III had the highest. The water absorption of Façade II was 28% and 37% lower than Façade I after 90 min and 24 h of wetting, respectively. Façade III had water absorption that was 1% lower and 11% higher than Façade I after the same time intervals. In the Karsten tube test, Façade II had 50% lower water absorption compared to Façade I. As depicted in Fig. 15, the water absorption of Façade II and I after 1 min was around 0 and 0.6 kg/m^2 , respectively. The latter value is comparable to the average water absorption of Façade I during 24 h of runoff wetting. The mass increase for Façade I after 90 min of Karsten tube wetting was around 4.0 kg/m^2 , while it was approximately 1.7 kg/m^2 and 0.35 kg/m^2 for capillary suction and runoff wetting,

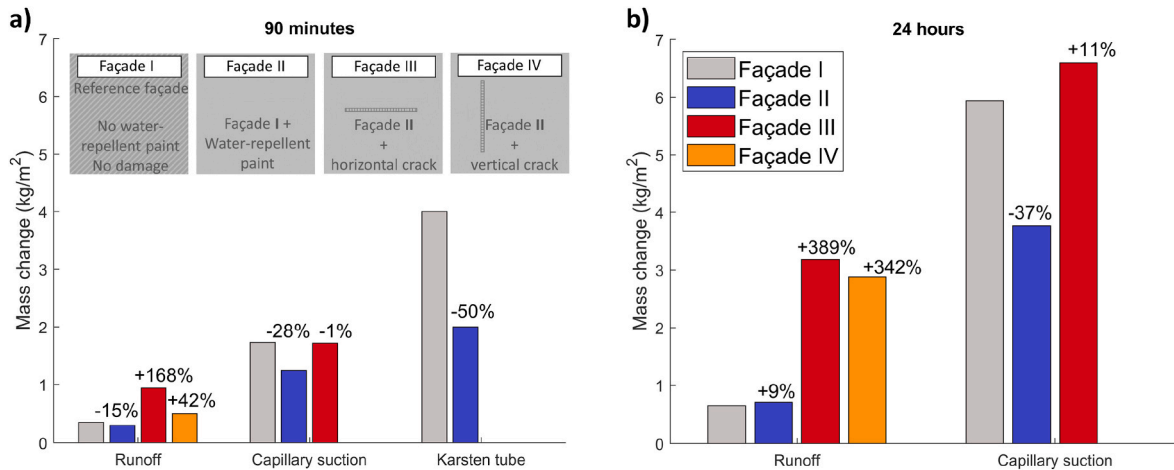


Fig. 16. Comparison of the maximum water absorption of Façades I-IV for different wetting scenarios, at short-term (a) and long-term (b). The relative mass gain between Façades II-IV and Façade I for the same wetting scenario is also provided. For the capillary suction test, the damaged façade was represented by Façade III only as the crack orientation was irrelevant. The Karsten tube tests only involved Façades I-II.

respectively. This implies that wetting with high pressure difference over the façade (1100 Pa) could result in 2–12 times greater water absorption compared to wetting with low hydrostatic pressure.

5. Discussions

5.1. Main study

As indicated in Chapter 1, previous test methods on the response of test walls to WDR normally involved a combination of high intensity water spraying and runoff, and high overpressure on the test walls. Meanwhile, the developed runoff setup was limited to water runoff, based on the most frequent WDR intensities in Sweden, and zero overpressure. Initial attempts were made to design water spray nozzles to mimic WDR. However, achieving the desired low intensities would necessitate dimming nozzles with small water droplet size and spread surface area, requiring multiple nozzles and a more complex monitoring system. Considering the first-time evaluation of the system used but also the potential uncertainties related to the increasing absorptivity of the ACM during subsequent wetting (reported in Ref. [51] and discussed in Chapter 1) the current version of the setup was limited to runoff wetting to mitigate these uncertainties. To compensate for this simplification, complementary studies were introduced to consider other wetting scenarios.

The reported moisture absorption (kg/m^2) of the specimens measured by the scale included the weight of the water runoff, which implies that the actual water absorption by the façade was lower than the reported values. Excluding the weight of the water film was challenging due to its variability. The maximum weight of the water film after 24 h of wetting was 0.08–0.011 kg/m^2 . In future studies, installing a second scale to measure the runoff water before it returns to the water tank could be a potential solution to address this issue. Furthermore, there exists a need for in-depth exploration regarding the water rivulet formation pattern and the specific timeframe for the emergence of the water film on the surface. Dyed water testing was conducted for visualizing the water stream on the surface. However, it failed due to the prolonged wetting phase, which not only removed or weakened the dyed areas but also distributed the dye in a transversal direction on the surface, making it challenging to distinguish the rivulet formation over time. Similarly, the observed variation in mass change between the measurement rounds for the undamaged façades (Fig. 9), in relation to the water film mass and measurement errors should be further investigated.

Both the hanging scale and moisture tracing sensors consistently

captured the response of the façades with satisfactory accuracy. The sensors had a total variability of 3–15% RH across all six measurement rounds, which could be attributed to the inherent variability of the measurement rounds and sensor errors. In future work, the sampling rate and resolution of the analogue to digital converter (ADC) used for the moisture tracing sensors could be improved by either using an ADC with a higher bit length (currently 10-bit) or using an amplifier.

In some measurement rounds, the damaged façades exhibited notable greater water absorption through the cracks, and negligible in others. This suggests that a theoretically large crack may not always lead to substantial water absorption, especially in pure rainwater runoff scenarios. These variations could be attributed to factors such as the presence of a water film at the crack opening, surface conditions, and the position of the crack relative to the water supply pipe. The effect of these parameters was not explored in this study. Furthermore, alternative techniques mentioned for inducing cracks with diminished impact on the surrounding surface and potentially larger number of samples should be investigated.

As shown in Table 1, the increase in thermal conductivity of the ACM is less than 13% up to 80% RH compared to dry state. In undamaged façades, the RH behind the ACM remained below 70% for 24 h of wetting, indicating a minimal impact on its thermal performance. However, in damaged façades with the highest moisture absorption (Fig. 12), the RH behind the ACM could locally reach values of 85–95%, which can lead to an 80–88% increase in thermal conductivity. This extreme case emphasizes the need to control water absorption for maintaining the insulation properties of the ACM. Long-term hygrothermal analyses should consider the possibility of damage due to cracking in ACM-systems, as discussed in Chapter 1.

The simulations underestimated the total moisture absorption and RH behind the outer mortar, possibly due to the simplified transport phenomena and boundary conditions. The model assumed a wet and saturated exterior surface instead of a water film, which would better represent the actual capillary suction at the surface. The inclusion of water runoff weight in the measurements may have contributed to differences between measured and simulated values. During drying, predicted values fell within the lower range of measured values, underestimating by 14–25% compared to the mean values. The simulations showed delayed RH predictions and slower drying rates, likely due to uncertainties in the moisture transport coefficients, ACM's sorption isotherm, moisture buffering capacity, and hysteresis effects. Additional parametric studies, including meshing and boundary condition modifications, did not significantly improve the agreement between simulations and experimental data. The results highlight the need for

further model calibration and refinement. Further investigation, among others, consideration of other driving potentials than relative humidity, such as partial vapor pressure or logarithmic of suction pressure, and consideration of different material properties at wetting and drying phases should be considered.

5.2. Complementary studies

The study in Ref. [51] showed a significant increase in capillary water absorptivity of the ACM after three rounds of 90-min tests. In this paper, similar tests were conducted on a ACM-system with the same ACM used in Ref. [51]. The results revealed a maximum increase of up to 5% after three rounds of 90-min wetting and below 13% after 24 h of wetting. Meanwhile, the coefficient of variance ranged from 3% to 28%, indicating a relatively high uncertainty in the testing method, particularly related to manual weighing. Despite the moderate increase after three rounds, these findings suggest that the ACM-system exhibits a more stable performance compared to the ACM as a stand-alone material. Nonetheless, further research with a greater number of wetting rounds is needed to assess the long-term performance of the ACM and the ACM-system.

The Karsten tube test is an effective and handy method to test the response of specimens to high-pressure wetting. However, there are several uncertainties inherent to the method that may impact the outcome. The small amount of water used, and the visual assessment of water absorption may lead to imprecise readings. The small contact area (300 mm²) of the tube may not represent the entire wall surface, and variations in attachment of the tube to the wall surface can further impact the results. Conducting a large number of tests can help mitigate these uncertainties.

6. Conclusion

This paper studied the moisture absorption of a coating system with an aerogel-based coating mortar (ACM-system) under three wetting scenarios. Specimens of the ACM-system with different surface conditions were studied, including cracks and water-repellent paint. A practical and small-scale runoff setup was developed in-house to continuously and in real-time monitor the moisture absorption and drying of the ACM-system. The results from short-term (90 min) and long-term (24 h) runoff wetting, as well as 144 h of initial drying, were analyzed. Additionally, two complementary studies, capillary suction and Karsten tube tests, were performed to measure the water absorption of the ACM-system under wetting conditions other than those in the runoff setup. Alongside the experimental investigations, an attempt was made to validate a simplified numerical hygrothermal model using the runoff wetting experiment, with the aim of facilitating future numerical studies.

Based on the obtained results, the conclusions are as follow.

- Among the three wetting scenarios, runoff wetting resulted in the lowest moisture absorption by the ACM-system for both short-term (90 min) and long-term (24 h) wetting. In short-term, the Karsten tube wetting showed 2–12 times higher absorption compared to the runoff and capillary suction wetting.

- The impact of water-repellent paint on moisture absorption and drying performance of the ACM-system was found to be less significant for runoff wetting ($\pm 9\%$). However, for capillary suction and Karsten tube wetting, it could reduce water absorption by up to 15% and 50%, respectively.
- For a damaged ACM-system with a horizontal or vertical surface crack of 1 ± 0.5 mm width, the hydrostatic pressure resulting from the runoff water film alone could increase water absorption by 3–5 times during long-term wetting. This could lead to prolonged drying time and potentially over 80% higher thermal conductivity compared to when dry.
- For an undamaged ACM-system, external drying can be sufficient to remove absorbed moisture from runoff wetting and prevent moisture accumulation if internal drying is prevented. However, a damaged ACM-system with a surface crack may require longer drying, and risk localized moisture accumulation if internal drying is restricted.
- During three consecutive rounds of runoff wetting and capillary suction, the ACM-system exhibited a modest rise (up to 13%) in water absorptivity. This finding implies a significantly more consistent performance of the ACM-system compared to the increase (260% [51]) observed for the ACM when used as a stand-alone material.
- The simplified numerical simulation model developed showed less satisfactory agreement with experimental data, highlighting the need for further model refinement and more advanced modeling of moisture transport in the ACM-system.
- The developed small-scale runoff setup and the integrated monitoring systems showed promising results for measuring moisture conditions in the specimens at wetting and drying. The measurements obtained from the setup can be effectively used to validate hygrothermal simulations in future investigations.

Funding

This work was supported by the Swedish Energy Agency [46822-1 & P2022-00872]. The practical support by Sebastian Almfeldt and Anders Karlsson during the development of the runoff setup is acknowledged.

CRediT authorship contribution statement

Ali Naman Karim: Writing – review & editing, Writing – original draft, Visualization, Validation, Methodology, Investigation, Formal analysis, Data curation, Conceptualization. **Angela Sasic Kalagasidis:** Writing – review & editing, Supervision, Conceptualization. **Pär Johansson:** Writing – review & editing, Supervision, Project administration, Funding acquisition, Conceptualization.

Declaration of competing interest

The authors declare that they have no known competing financial interests or personal relationships that could have appeared to influence the work reported in this paper.

Data availability

Data will be made available on request.

Appendix A. Dimensioning of the water supply system in the runoff setup

In the runoff setup, the water system was designed to replicate the maximum runoff intensity on the windward façade of a 15-m-tall, three-story building, considering the most frequent WDR intensities in Sweden. First, historical and hourly data on rain intensities and wind velocities were collected for eight Swedish cities spanning a 25-year period. Second, the WDR intensities striking the façade were calculated according to EN ISO 15927-3 [15]. Finally, the method proposed by Blocken and Carmeliet [13] was used to estimate the maximum runoff intensity.

A.1. Rain intensities and wind velocities

Hourly rain and wind data were collected from the Swedish Meteorological and Hydrological Institute (SMHI) [72] for the period 1996–2021. The data was obtained from eight weather stations (Figure A 1) selected to represent various geographical locations in Sweden with a denser selection in the south and west, where WDR events are more prevalent.



Fig. A 1. Map of Sweden (red marks, source: Google Earth) and the locations of the selected weather stations.

Figure A 2 and Figure A 3 present the hourly maximum and most frequent (95th percentile confidence interval) rain intensities and wind velocities, respectively. The highest rain intensities varied from 20 to 40 mm/h ($L/(h \cdot m^2)$), whereas the most frequent rain events had intensities less than 3 mm/h. The maximum wind velocities were between 10 and 20 m/s, and the most frequent wind velocities were below 7 m/s. Most rain events were less than 5 h in duration, with longer events (longer than 10 h) being uncommon. In the subsequent analyses, the most frequent rain and wind intensities, 3 mm/h and 7 m/s, respectively, were considered.

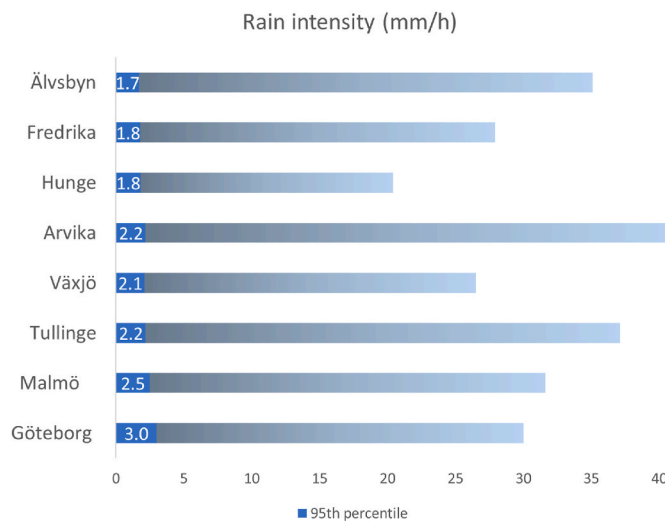


Fig. A 2. Rain intensities (hourly maximum and 95th percentile) between 1996 and 2021.

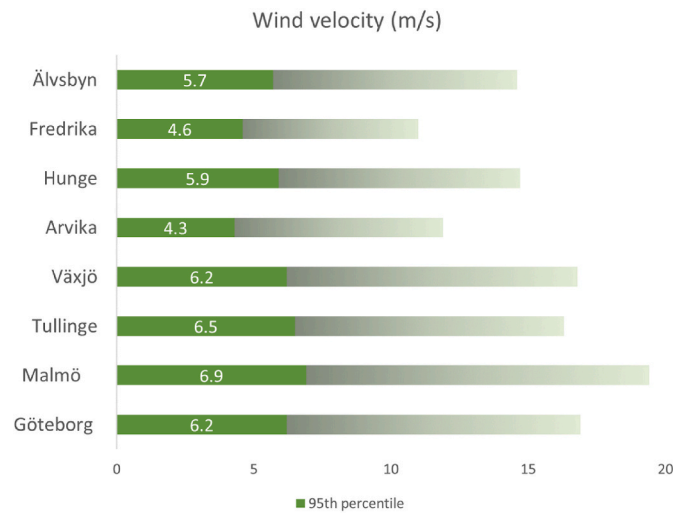


Fig. A 3. Wind velocities (hourly maximum and 95th percentile) between 1996 and 2021.

A.2. Estimation of WDR on a vertical wall

The standard EN ISO 15927-3 [15] outlines a method for calculating the WDR intensity impacting on a vertical façade based on hourly rain intensity and wind velocity measurements. Originally developed for calculating annual average WDR intensities, Blocken and Carmeliet [73] suggest its applicability to shorter time periods. Here, the key aspects of the method [15] are introduced.

The formula for calculating the WDR intensity, I_{WDR} (L/m^2), impacting a vertical wall surface is as follows [15]:

$$I_{WDR} = I_A \cdot C_R \cdot C_T \cdot O \cdot W \quad (A.1)$$

$$I_A = \frac{2}{9} \cdot v \cdot r^{0.9} \cdot \cos(\Theta) \quad (A.2)$$

where v (m/s) is the hourly mean wind velocity, r (mm) is the hourly rainfall and Θ ($^\circ$) is the angle between the wind direction and the normal out of the vertical wall surface. C_R (–) and C_T (–) are the roughness and topography coefficients, O (–) is the obstruction factor and W (–) is the wall factor describing the quantity of rainwater impacting different parts of the wall. The calculation method and tabulated values for these parameters are presented in Ref. [15]. To explore all possible combinations of parameters for Equation A. 1 and A. 2, a parametric study was conducted (Table A 1).

Table A 1

Selected parameters for the analysis performed based on the method in Ref. [15].

Parameter	Values
v (m/s)	7
r (mm)	3
Θ ($^\circ$)	0, 45
C_R (–)	0.25–1.30
C_T (–)	1–1.6
O (–)	0.2, 0.5, 0.7, 1
W (–)	0.2, 0.3, 0.4, 0.5

Table A 2 summarizes the findings of the study. For further analyses, the WDR profile based on the 95th percentile values along the 15 m height of the façade was considered.

Table A 2

The calculated WDR intensity (mm/h) on the windward façade of a 15-m-tall building.

Height (m)	0	3	6	9	12	15
Maximum	0	1.3	2.2	2.3	3.2	4.1
Mean	0	0.3	0.5	0.6	0.8	1.1
Median	0	0.2	0.4	0.5	0.7	0.9
95th percentile	0	0.7	1.3	1.4	2.0	2.6

A.3. Estimation of runoff intensity

The numerical model proposed by Blocken and Carmeliet [13] was used to calculate the maximum runoff intensity due to WDR exposure on the façade. The model incorporated WDR impacting the façade as a source and capillary water absorption into the wall as a sink. Surface evaporation was not taken into account, assuming that high RH during rain would limit evaporation. The velocity profile of the water film flow due to water runoff on the façade was characterized in Ref. [13] by employing the parabolic velocity profile of the Nusselt solution as a simplified thin film flow. The model was presented as a first-order hyperbolic partial differential equation, with the water film thickness, h (mm), being the primary variable. From the water film thickness, the total water flow rate, q ($\text{m}^3/(\text{m} \cdot \text{s})$), passing a particular position on the façade at a given time could be computed. For detailed model specifications, refer to Ref. [13].

The water film velocity and flow rate are calculated by the Nusselt solution [13]:

$$q = \int_0^h u(y) dy = \frac{g_r \cdot h^3}{3 \cdot \nu} \cdot \sin \beta \quad (\text{A.3})$$

$$u = \frac{q}{h} = \frac{g_r \cdot h^2}{3 \cdot \nu} \cdot \sin \beta \quad (\text{A.4})$$

where $u(y)$ (m/s) is the streamwise and transverse water film velocity, ν (m^2/s) is kinematic viscosity, g_r (m^2/s) is gravitational acceleration, and β (degree) is wall inclination.

The water film thickness (h) at various positions along the vertical length of the façade (x -direction) at different times, t (s), are represented by Equation A.5 [13]. The corresponding discretized solution is presented in Equation A.6:

$$\frac{\partial h}{\partial t} + \frac{g_r \cdot h^2}{\nu} \frac{\partial h}{\partial x} = \frac{g_{\text{wdr}} - g_{\text{abs}}}{\rho} \quad (\text{A.5})$$

$$\frac{h_j^{n+1}}{\Delta t^{n+1}} + \frac{g_r}{3\nu} \cdot \left(\frac{(h_j^n)^3 - (h_{j-1}^n)^3}{\Delta x_{j-1}} \right) = \frac{(g_{\text{wdr}} - g_{\text{abs}})_j^{n+1}}{\rho} \quad (\text{A.6})$$

where g_{wdr} and g_{abs} ($\text{L}/(\text{m}^2 \cdot \text{s})$ or $\text{m}^3/(\text{m}^2 \cdot \text{s})$) are the WDR flux and the absorption flux, respectively. Finally, n and j represent the time- and space step on the façade, respectively.

A parametric study was conducted to evaluate the formation of water film and runoff on the analyzed façade from Section A.1 and A.2. The study involved numerically solving Equation A.6 through an explicit discretization scheme (forward difference in time and backward difference in space). The WDR profile from Section A.2 was used as g_{wdr} , while two cases were studied for g_{abs} based on the two types of façades considered in this paper. A low absorbent wall surface was considered based on Façade II (with water-repellent paint), with a capillary water absorption coefficient (A_{cap}) of $0.008 \text{ kg}/(\text{m}^2 \cdot \text{s}^{0.5})$. The second case was based on Façade I ($A_{\text{cap}} = 0.05 \text{ kg}/(\text{m}^2 \cdot \text{s}^{0.5})$). In all simulations, a constant A_{cap} was assumed along the total length of the façade assuming a uniformly dry/wet surface prior to the rainfall. The stability and convergence conditions described in Ref. [13] were satisfied by setting the space and time steps to 0.02 m and 0.02 s , respectively. The analyses were conducted for a 60-min-long rain event.

On the low absorbent façade, the water film formation was initiated with in few minutes from the start of the rain event, see Figure A 4. The maximum water film thickness was around 0.13 mm . For the more absorbent façade, the water film formation started after approximately 40 min at the upper parts of the façade. The maximum film thickness was calculated to be 0.095 mm . The maximum runoff flow rate along the length of the façade during the 1-h WDR event varied between 10 and 22 L/h . Therefore, the water supply system should be designed conservatively to maintain a constant water flow rate greater than 22 L/h .

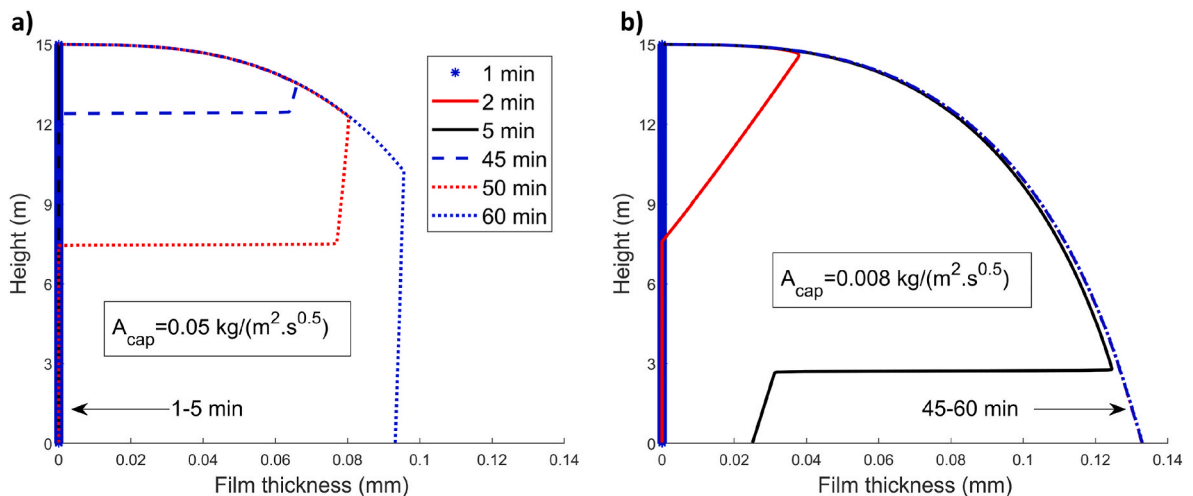


Fig. A 4. Water film thickness (h) profile for the two cases of high (a) and low (b) absorbent wall surfaces during a 1-h WDR event.

References

- [1] L. Olsson, Driving Rain Tightness, Intrusion Rates and Phenomenology of Leakages in Defects of Façades: A New Calculation Algorithm. PhD Thesis, Chalmers University of Technology, 2018.
- [2] S. Van Linden, Fourth Generation Watertightness: A Performance-Based Strategy to Control Rainwater Infiltration in Façade Systems, PhD Thesis, Ghent University, 2022.
- [3] N. Van Den Bossche, Watertightness of Building Components: Principles, Testing and Design Guidelines, PhD Thesis, Ghent University, 2013.
- [4] M. Lacasse, Recent Studies on the Control of Rain Penetration in Exterior Wood-Frame Walls, Natl. Res. Counc. Canada, 2003.
- [5] M.A. Lacasse, H. Miyauchi, J. Hiemstra, Water penetration of cladding components—results from laboratory tests on simulated sealed vertical and horizontal joints of wall cladding, *Artic J ASTM Int* (2009), <https://doi.org/10.1520/JAI102048>.
- [6] A.N. Karim, Aerogel-based plasters for renovation of buildings in Sweden: identification of possibilities, information deficiencies and challenges, Chalmers University of Technology (2021). Licentiate Thesis.
- [7] J. Straube, E.F.P. Burnett, Rain control and design strategies, *J. Therm. Envelope Build. Sci.* 23 (1999) 41–56, <https://doi.org/10.1177/109719639902300105>.
- [8] C. Svensson Tengberg, A Design-Build Contractor Risk Assessment Framework for New Technical Solutions in the Construction Industry, PhD Thesis, Chalmers University of Technology, 2022.
- [9] C. Svensson Tengberg, C.-E. Hagetoft, Risk assessment framework to avoid serial failure for new technical solutions applied to the construction of a CLT structure resilient to climate, *Buildings* 11 (2021) 247, <https://doi.org/10.3390/buildings11060247>.
- [10] Morrison Hershfield Ltd, Survey of Building Envelope Failures in the Coastal Climate of British Columbia, Canada Mortg Hous Corp BC Yukon Reg Off, 1996.
- [11] A.H. Buchanan, B.L. Deam, M. Fragiocomo, H. Morris, S. Tutor, Fifteen Years of Performance-Based Design in New Zealand, 2006.
- [12] B. Blocken, J. Carmeliet, A review of wind-driven rain research in building science, *J. Wind Eng. Ind. Aerod.* 92 (2004) 1079–1130, <https://doi.org/10.1016/J.JWEIA.2004.06.003>.
- [13] B. Blocken, J. Carmeliet, A simplified numerical model for rainwater runoff on building façades: possibilities and limitations, *Build. Environ.* 53 (2012) 59–73, <https://doi.org/10.1016/J.BUILDENV.2012.01.010>.
- [14] S. Van Linden, N. Van Den Bossche, Review of rainwater infiltration rates in wall assemblies, *Build. Environ.* 219 (2022), <https://doi.org/10.1016/J.BUILDENV.2022.109213>.
- [15] EN ISO 15927-3, Hygrothermal Performance of Buildings – Calculation and Presentation of Climatic Data – Part 3: Calculation of a Driving Rain Index for Vertical Surfaces from Hourly Wind and Rain Data, 2009.
- [16] H.M. Künzel, Simultaneous Heat and Moisture Transport in Building Components: One- and Two-Dimensional Calculation Using Simple Parameters. PhD Thesis, IRB Verlag Stuttgart, 1995.
- [17] ASHRAE, Standard 160-2016. Criteria for Moisture-Control Design Analysis in Buildings, ASHRAE, Atlanta, GA, 2016.
- [18] EN 1027, Windows and Doors – Water Tightness – Test Method, 2016.
- [19] EN 12865, Hygrothermal Performance of Building Components and Building Elements – Determination of the Resistance of External Wall Systems to Driving Rain under Pulsating Air Pressure, 2001.
- [20] S. Kahangi Shahreza, J. Niklewski, M. Molnár, Experimental investigation of water absorption and penetration in clay brick masonry under simulated uniform water spray exposure, *J. Build. Eng.* 43 (2021), 102583, <https://doi.org/10.1016/J.JOBE.2021.102583>.
- [21] S. Kahangi Shahreza, J. Niklewski, M. Molnár, Novel water penetration criterion for clay brick masonry claddings, *Construct. Build. Mater.* 353 (2022), 129109, <https://doi.org/10.1016/J.CONBUILDMAT.2022.129109>.
- [22] M.A. Lacasse, S. Cornick, A review of climate loads relevant to assessing the watertightness performance of walls, Windows, and Wall-Window interfaces 2 (2005) 1–16, <https://doi.org/10.1520/JAI12505>.
- [23] J. Straube, J.F. Straube, E.F.P. Burnett, Simplified prediction of driving rain on buildings, in: *Proc. Int. Build. Phys. Conf.*, Eindhoven University of Technology Eindhoven, the Netherlands, 2000.
- [24] N. Sahal, M.A. Lacasse, Proposed method for calculating water penetration test parameters of wall assemblies as applied to Istanbul, Turkey, *Build. Environ.* 43 (2008) 1250–1260, <https://doi.org/10.1016/J.BUILDENV.2007.03.009>.
- [25] J.M. Pérez-Bella, J. Domínguez-Hernández, E. Cano-Suñén, J.J. del Coz-Díaz, F. J. Suárez-Domínguez, A comparison of methods for determining watertightness test parameters of building façades, *Build. Environ.* 78 (2014) 145–154, <https://doi.org/10.1016/J.BUILDENV.2014.04.027>.
- [26] N. Van Den Bossche, M.A. Lacasse, A. Janssens, A uniform methodology to establish test parameters for watertightness testing: Part I: a critical review, *Build. Environ.* 63 (2013) 145–156, <https://doi.org/10.1016/J.BUILDENV.2012.12.003>.
- [27] N. Van Den Bossche, M.A. Lacasse, A. Janssens, A uniform methodology to establish test parameters for watertightness testing part II: pareto front analysis on co-occurring rain and wind, *Build. Environ.* 63 (2013) 157–167, <https://doi.org/10.1016/J.BUILDENV.2012.12.019>.
- [28] A.N. Karim, P. Johansson, A. Sasic Kalagasidis, Knowledge gaps regarding the hygrothermal and long-term performance of aerogel-based coating mortars, *Construct. Build. Mater.* 314 (2022), 125602, <https://doi.org/10.1016/J.CONBUILDMAT.2021.125602>.
- [29] H. Maleki, Recent advances in aerogels for environmental remediation applications: a review, *Chem. Eng. J.* 300 (2016) 98–118, <https://doi.org/10.1016/J.CEJ.2016.04.098>.
- [30] N. Gaponik, A.K. Herrmann, A. Eychmüller, Colloidal nanocrystal-based gels and aerogels: material aspects and application perspectives, *J. Phys. Chem. Lett.* 3 (2012) 8–17, <https://doi.org/10.1021/jz201357r>.
- [31] A. Soleimani Dorcheh, M.H. Abbasi, Silica aerogel: synthesis, properties and characterization, *J. Mater. Process. Technol.* 199 (2008) 10–26, <https://doi.org/10.1016/J.jmatprotec.2007.10.060>.
- [32] H. Maleki, L. Duraes, C.A. García-González, P. del Gaudio, A. Portugal, M. Mahmoudi, Synthesis and biomedical applications of aerogels: possibilities and challenges, *Adv. Colloid Interface Sci.* 236 (2016) 1–27, <https://doi.org/10.1016/J.CIS.2016.05.011>.
- [33] A. Lamy-Mendes, A.D.R. Pontinha, P. Alves, P. Santos, L. Duraes, Progress in silica aerogel-containing materials for buildings' thermal insulation, *Construct. Build. Mater.* 286 (2021), 122815, <https://doi.org/10.1016/J.CONBUILDMAT.2021.122815>.
- [34] C. Li, G. Zhang, L. Lin, T. Wu, S. Brunner, S. Galmarini, et al., Silica aerogels: from materials research to industrial applications, *Int. Mater. Rev.* (2023) 1–39, <https://doi.org/10.1080/09506608.2023.2167547>.
- [35] C.V. Fiorini, F. Merli, E. Belloni, M.K. Carroll, A.M. Anderson, C. Buratti, Long-term performance of monolithic silica aerogel with different hydrophobicities: physical and color rendering properties after an accelerated aging process, *Gels* 9 (2023), <https://doi.org/10.3390/gels9030210>.
- [36] M. Ibrahim, E. Wurtz, P.H. Biwale, P. Achard, H. Sallee, Hygrothermal performance of exterior walls covered with aerogel-based insulating rendering, *Energy Build.* 84 (2014) 241–251, <https://doi.org/10.1016/J.ENBUILD.2014.07.039>.
- [37] M. Ibrahim, P.H. Biwale, P. Achard, E. Wurtz, G. Ansart, Building envelope with a new aerogel-based insulating rendering: experimental and numerical study, cost analysis, and thickness optimization, *Appl. Energy* 159 (2015) 490–501, <https://doi.org/10.1016/J.APENERGY.2015.08.090>.
- [38] M. Ibrahim, P.H. Biwale, E. Wurtz, P. Achard, A study on the thermal performance of exterior walls covered with a recently patented silica-aerogel-based insulating coating, *Build. Environ.* 81 (2014) 112–122, <https://doi.org/10.1016/J.BUILDENV.2014.06.017>.
- [39] T. Stahl, K. Ghazi Wakili, S. Hartmeier, E. Franov, W. Niederberger, M. Zimmermann, Temperature and moisture evolution beneath an aerogel based rendering applied to a historic building, *J. Build. Eng.* 12 (2017) 140–146, <https://doi.org/10.1016/J.JOBE.2017.05.016>.
- [40] E. Fenoglio, S. Fantucci, M. Perino, V. Serra, M. Dutto, V. Marino, Energy retrofit of residential buildings with a novel super-insulating aerogel-based plaster, *AICARR J* 61 (2020) 44–48.
- [41] K. Ghazi Wakili, C. Dworatzky, M. Sanner, A. Sengespeick, M. Paronen, T. Stahl, Energy efficient retrofit of a prefabricated concrete panel building (Plattenbau) in Berlin by applying an aerogel based rendering to its façades, *Energy Build.* 165 (2018) 293–300, <https://doi.org/10.1016/J.ENBUILD.2018.01.050>.
- [42] S. Fantucci, E. Fenoglio, G. Grosso, V. Serra, M. Perino, M. Dutto, et al., Retrofit of the existing buildings using a novel developed aerogel-based coating: results from an in-field monitoring, in: *7th Int. Build. Phys. Conf. IBPC2018*, Syracuse University Libraries, 2018, pp. 283–288, <https://doi.org/10.14305/ibpc.2018-be-7.06>.
- [43] K. Ghazi Wakili, T. Stahl, E. Heiduk, M. Schuss, R. Vonbank, U. Pont, et al., High performance aerogel containing plaster for historic buildings with structured façades, *Energy Proc.* 78 (2015) 949–954, <https://doi.org/10.1016/j.egypro.2015.11.027>.
- [44] S. Ximenes, A. Silva, A. Soares, I. Flores-Colen, J. de Brito, Parametric analysis to study the influence of aerogel-based renders' components on thermal and mechanical performance, *Materials* 9 (2016), <https://doi.org/10.3390/ma9050336>, 336–255.
- [45] T. Stahl, K.G. Wakili, E. Heiduk, Stability relevant properties of an SiO₂ aerogel-based rendering and its application on buildings, *Sustain. Times* 13 (2021), 10035, <https://doi.org/10.3390/SU131810035>, 10035 2021;13.
- [46] M. Guizzardi, Hygrothermal Performance Assessment of Novel Interior Insulation Solutions, PhD Thesis, ETH Zurich, 2014, <https://doi.org/10.3929/ethz-a-010277871>.
- [47] M. Guizzardi, D. Derome, D. Mannes, R. Vonbank, J. Carmeliet, Electrical conductivity sensors for water penetration monitoring in building masonry materials, *Mater Struct Constr* 49 (2016) 2535–2547, <https://doi.org/10.1617/s11527-015-0666-7>.
- [48] M. Guizzardi, D. Derome, R. Vonbank, J. Carmeliet, Hygrothermal behavior of a massive wall with interior insulation during wetting, *Build. Environ.* 89 (2015) 59–71, <https://doi.org/10.1016/J.BUILDENV.2015.01.034>.
- [49] N.R.M. Sakiyama, J. Frick, M. Stipetic, T. Oertel, H. Garrecht, Hygrothermal performance of a new aerogel-based insulating render through weathering: impact on building energy efficiency, *Build. Environ.* 202 (2021), 108004, <https://doi.org/10.1016/j.buildenv.2021.108004>.
- [50] J. Maia, M. Pedrosa, N.M.M. Ramos, I. Flores-Colen, P.F. Pereira, L. Silva, Durability of a new thermal aerogel-based rendering system under distinct accelerated aging conditions, *Materials* 14 (2021) 5413, <https://doi.org/10.3390/MA14185413>, 5413 2021;14.
- [51] A.N. Karim, P. Johansson, A.S. Kalagasidis, Increasing water absorptivity of an aerogel-based coating mortar in subsequent wetting and drying, *Gels* 8 (2022) 764, <https://doi.org/10.3390/GELS8120764>, 764 2022;8.

- [52] K. Sandin, Beständighet hos putsade fasader : probleminventering, Rapport TVBM 3079 (1998) (Durability of rendered facades: problem inventory). [In Swedish]. Division of Building Materials, Lund University.
- [53] M. Hassanzadeh, Sprickbildning i puts på isolering - undersökning av grundläggande mekanismer, Rapport TVBM 3117 (2004) (Crack propagation in render on insulation- investigation of basic mechanisms). [In Swedish]. Division of Building Materials, Lund University.
- [54] M. Molnar, J. Jönsson, K. Sandin, T. Gustavsson, Undvik Misstag I Murat Och Putsat Byggande. SBUF 12983 Slutrapport (Avoid Mistakes in Masonry and Rendered Constructions. SBUF 12983 Final Report), SBUF Svenska byggbranschens utvecklingsfond, 2006 [In Swedish].
- [55] K. Sandin, Vattenavvisande fasadimpregnering (Water repellent facade treatment), Division of Building Materials, Lund University (1993) [In Swedish].
- [56] J. Jönsson, P. Rosenkvist, M. Molnár, Undersökning Av Vatteninträngning I Tilläggsisoleringssystem Av Mineralull Och Tjockputs- Resultat Från Laboratiestudier (Investigation of Water Penetration in Mineral Wool and Thick Render Insulation Systems- Results of Laboratory Studies), Division of Structural Engineering, Lund University, 2016 [In Swedish].
- [57] K. Wang, D.C. Jansen, S.P. Shah, A.F. Karr, Permeability study of cracked concrete, *Cement Concr. Res.* 27 (1997) 381–393, [https://doi.org/10.1016/S0008-8846\(97\)00031-8](https://doi.org/10.1016/S0008-8846(97)00031-8).
- [58] S.S. Park, S.J. Kwon, S.H. Jung, S.W. Lee, Modeling of water permeability in early aged concrete with cracks based on micro pore structure, *Construct. Build. Mater.* 27 (2012) 597–604, <https://doi.org/10.1016/J.CONBUILDMAT.2011.07.002>.
- [59] A. Akhavan, S.M.H. Shafaatian, F. Rajabipour, Quantifying the effects of crack width, tortuosity, and roughness on water permeability of cracked mortars, *Cement Concr. Res.* 42 (2012) 313–320, <https://doi.org/10.1016/J.CEMCONRES.2011.10.002>.
- [60] V. Mechtcherine, M. Lieboldt, Permeation of water and gases through cracked textile reinforced concrete, *Cem. Compos.* 33 (2011) 725–734, <https://doi.org/10.1016/J.CEMCONCOMP.2011.04.001>.
- [61] M. Hassanzadeh, Sprickbildning i puts på isolering : inledande laboratorieförsök och parameterstudier, Rapport TVBM 3099 (2001) (Crack propagation in render on insulation : initial laboratory tests and parameter studies). [In Swedish]. Division of Building Materials, Lund University.
- [62] K. Sandin, Sprickbildning i puts på isolering : inledande studier av putsens krympning och svällning, Rapport TVBM 3101 (2002) (Crack propagation in render on insulation: initial studies on shrinkage and swelling of render). [In Swedish]. Division of Building Materials, Lund University.
- [63] S. Van Linden, M. Lacasse, N. Van, D. Bossche, Drainage of Infiltrated Rainwater in Wall Assemblies: Test Method, Experimental Quantification, and Recommendations, *Res Pap J Build Phys* n.d., 2022, pp. 1022–1056, <https://doi.org/10.1177/17442591221121932>.
- [64] Wall Systems, HECK AERO iP, 2022. <https://www.wall-systems.com/produkte/daemmputze-innendaemmung/aero-ip>. (Accessed 23 October 2022).
- [65] ISO 22007-2. Plastics — Determination of Thermal Conductivity and Thermal Diffusivity — Part 2: Transient Plane Heat Source (Hot Disc) Method, 2015.
- [66] EN 1015-19, Methods of Tests for Mortar for Masonry – Part 19: Determination of Water Vapour Permeability of Hardened Rendering and Plastering Mortars, 1999.
- [67] EN 1015-18, Methods of Test for Mortar for Masonry – Part 18: Determination of Water Absorption Coefficient Due to Capillary Action of Hardened Mortar, 2002.
- [68] EN ISO 12571, Hygrothermal Performance of Building Materials and Products – Determination of Hygroscopic Sorption Properties, 2013.
- [69] Draft recommendation for in situ concrete strength determination by combined non-destructive methods, *Mater. Struct.* 26 (1993) 43–49, <https://doi.org/10.1007/BF02472237>.
- [70] LNEC (National Laboratory of Civil Engineering), Wall Coatings. Water Absorption Test under Low Pressure (In Portuguese), 2002. Lisbon, Portugal.
- [71] LNEC (National Laboratory of Civil Engineering), In-situ Tests on Wall Coatings for Old Buildings. Preliminary Tests with Karsten Tubes, 2002 (In Portuguese). Lisbon, Portugal.
- [72] SMHI, Ladda ner meteorologiska observationer. <https://www.smhi.se/data/meteorologi/ladda-ner-meteorologiska-observationer#param=precipitationHourlySum,stations=all,stationid=161910>, 2021. (Accessed 15 September 2021).
- [73] B. Blocken, J. Carmeliet, Overview of three state-of-the-art wind-driven rain assessment models and comparison based on model theory, *Build. Environ.* 45 (2010) 691–703, <https://doi.org/10.1016/J.BUILDENV.2009.08.007>.